Chronology of sedimentation and landscape evolution in the Okavango Rift Zone, a developing young rift in southern Africa

S. Vainer[1,2]*, C. Schmidt[1], E. Garzanti[3], Y. Ben Dor[4], G. Pastore[3], T. Mokatse[1], C. Prud'homme[1,5], L. Leanni[6], G. King[1], ASTER Team[6]†, E. P. Verrecchia[1,7]

[1]Institute of Earth Surface Dynamics, University of Lausanne, 1015 Lausanne, Switzerland. [2]GET (Université de Toulouse, CNRS, IRD, UPS, CNES), 31400 Toulouse, France. [3]Department of Earth and Environmental Sciences, University of Milano-Bicocca, 20126 Milano, Italy. [4]Geological Survey of Israel, 32 Yesha'yahu Leibowitz, Jerusalem 9692100, Israel. [5]Centre de Recherches Pétrographiques et Géochimiques, Université de Lorraine, CNRS, 54500 Vandœuvre-lès-Nancy, France. [6]Aix-Marseille Université, CNRS, Collège de France, IRD, INRA, CEREGE, 13545 Aix-en-Provence, France. [7]Earth and Environmental Sciences, Botswana International University of Science and Technology, Palapye, Botswana

*Corresponding author: Shlomy Vainer (shlomy.vainer@mail.huji.ac.i)

† Group separate identification: Georges Aumaître, Didier L. Bourlès & Karim Keddadouche

Key Points:

- Nascent continental rifting stages are reflected through sedimentological variations
- Eolian sand that was formed prior to alluvial incision into the rift is preserved on elevated surfaces
- Depositional environments in the incised rift have shifted into alluvial-lacustrine conditions around the Middle Pleistocene Transition

Abstract

The Kalahari Basin in southern Africa, shaped by subsidence and epeirogeny, features the Okavango Rift Zone (ORZ) as a significant structural element characterized by diffused extensional deformation forming a prominent depocenter. This study elucidates the Pleistocene landscape evolution of the ORZ by examining the chronology of sediment formation and filling this incipient rift and its surroundings.

Modeling of cosmogenic nuclide concentrations in surficial eolian sand from distinct structural blocks around the ORZ provides insights into sand's residence time on the surface. Sand formation occurred from ~2.2 to 1.1 Ma, coinciding with regional tectonic events. Notably, provenance analyses of sand within ORZ's lowermost block where large alluvial fans are found indicate different source rocks and depositional environments than those of the more elevated eolian sand. This suggests that the major phase of rift subsidence and the following incision of alluvial systems into the rift occurred after eolian dune formation. Luminescence dating reveals that deposition in alluvial fan settings in the incised landscape began not later than ~250 ka, and that a lacustrine environment existed since at least ~140 ka.

The established chronological framework constrains the geomorphological effects of the different tectono-climatic forces that shaped this nascent rifting area. It highlights two pronounced stages of landscape development, with the most recent major deformation event in

the evolving rift probably occurring during the middle Pleistocene transition (1.2-0.75 Ma). This event is reflected as a striking change in the depositional environments due to the configurational changes accompanying rift progression.

Plain Language Summary

Early stages of continental rifting in the Okavango Rift Zone are described from the perspective of sediment dynamics by constructing a time frame for their evolution. Two major types of sediment and their corresponding time scales are studied. The older sediments are eolian sands that were formed between ~2.2 and 1.1 million years ago, lying today on elevated structural surfaces above the incised rift. Within the subsidized rift that was geomorphologically modified not earlier than 1 million years ago, sediments were deposited by alluvial fans at least since 250 thousand years ago, and were followed by a lacustrine environment with alternating hydrological conditions, since at least 140 thousand years ago.

1. Introduction

Tectonic geomorphology incorporates various disciplines and is an evolving field with recent advances in geochronological methods (Keller and DeVecchio 2013; Owen, 2022). While numeric age determinations are being widely used to reconstruct and quantify landscape evolution, multiple processes are involved in the buildup of the analyzed proxies such that their interpretation must be consistent with the geomorphologic context (Watchman and Twidale, 2002; Le Dortz et al., 2012; Brown, 2020). Among the most studied features for elucidating and evaluating the effects of tectonics and climate on landscape evolution are alluvial and fluvial subaerial fans, which are common also in rift settings and experience a highly dynamic geomorphological history (Gierlowski-Kordesch, 2010; Warren; 2010; Scheinert et al., 2012; Bowman, 2019).

Subaerial fans are generally found and best preserved at the base of mountain fronts within tectonically active zones, where changes in base level are induced by tectonics and variations in climate (Harvey, 2002; Blair and McPherson, 2009). Extensive research has been performed to study their morphologies, involved processes and mechanisms, as well as the components within the system (e.g., nature of sediments, vegetation, lithology) and to reconcile the respective roles of climate and tectonics in their formation (Lustig, 1965; Hooke, 1967; Ritter et al., 1995; Viseras et al., 2003; Terrizzano et al., 2017; Harvey et al., 2018; Bowman, 2019). Multiple models for the environmental evolution of fans were formulated based on disparate methods and over a biased global spatial distribution and settings as most of the primary studies were conducted in the American southwest (Lecce, 1990; Scheinert et al., 2012; Stock, 2013).

The Okavango Rift Zone (ORZ; Figure 1), in interior southern Africa, constitutes an intriguing area to study tectonic geomorphology through the stages involved in the development of alluvial fans and lacustrine/palustrine environments during nascent rifting (Scholz et al., 1976; Kinabo et al., 2007; Wright et al., 2021; Paulssen et al., 2022), where globally unique megafans and paleo-lakes are preserved (Shaw and Thomas, 1992; Burrough and Thomas, 2013). Paleo-lacustrine environments have been thoroughly studied in this area (Moore et al., 2012 and references therein) but, apart from the numerous studies of the Okavango Delta (Podgorski et al., 2013; McCarthy, 2013 and references therein), little attention has been given to the early evolution of fans in central southern Africa (Blair and McPherson, 2009; Wilkinson et al., 2023). Moreover,

as the ORZ is bordered by eolian dunes and was subjected to varying zonal climatic interactions (Partridge, 1993; Shaw and Thomas, 1988; Burrough and Thomas, 2013), chronological constraints of landscape evolution that precede the most recent eolian deposition stages are rare (Moore et al., 2012; McCarthy, 2013; Vainer et al., 2021). Therefore, as favored in other regions and settings where recent and earlier fans were studied and compared (DeCelles and Cavazza, 1999; Harvey et al., 2005), an investigation of previous phases of landscape development along the ORZ is required.

The ORZ lies within the largest continuous sand sheet on Earth and preserves remnants of vast waterbodies (Figure 2) (Grove, 1969; Baillieul 1975; Burrough and Thomas, 2013; McCarthy, 2013; Wilkinson et al., 2023). The largest active fan within the ORZ, the Okavango Delta), is characterized by the lowest slope gradient of any other studied subaerial fan and defines one out of three end members of fan types, representing the “losimean” character which is governed by anastomosing meanders (Stanistreet and McCarthy 1993; Bowman, 2019; Wright et al., 2021). Although the Okavango Delta is one of the largest alluvial fans in Africa (McCarthy, 1993) and comprises today the most active depocenter in the Kalahari Basin (Figure 1), isopach maps reveal that, the main depocenter in the Okavango Basin lies ~100 km to the northeast of the Okavango Delta (Figure 3). This area occupies the Linyanti-Chobe Basin within the Chobe Enclave (CE) (Figure 2), which hosts a large alluvial fan that is partially truncated due to tectonic activity (Shaw and Thomas, 1992; McCarthy, 2013; Mokatse et al., 2022a; Wilkinson et al., 2023).

While chronological studies of alluvial fans' evolution have shed light on the relationships between their development and tectonics (e.g. Matmon et al., 2006; Placzek et al., 2010; Porat et al., 2010; Terrizzano et al., 2017), the affinity between tectonic settings and eolian accumulation and preservation is poorly constrained and largely unquantified (Cosgrove et al., 2022). Furthermore, it has been postulated that not all fan surfaces are suitable to be dated, particularly at sites where signs of weathering, reworking, and changes in sources are evident (Watchman and Twidale, 2002; Matmon et al., 2005). Due to the prevalence of these processes in the CE (Garzanti et al., 2022) and the uncertainties of available chronological constraints (Moore et al., 2012; McCarthy, 2013), an adjustment of conventional dating methods is needed to construct a chronological framework of this terrane.

This study constructs a temporal framework of the geomorphological response to the incipient rifting stages of the ORZ, the southwestern most part of the East African Rift System (EARS). Along the related segments of this rifting system, the latest age constraints for down-warping and faulting are of Pliocene age (Figure 1; Michon et al., 2022). Therefore, rift-related deformation in the ORZ is expected to occur from the Pliocene onwards. Following this assumption, we apply luminescence-based chronologies of buried deposits of the Cuando Megafan, lying in the heart of the ORZ (i.e., CE), with cosmogenic nuclide-based residence time estimates of the surrounding regional eolian sand (Figure 2). These chronometers cover together three relevant temporal orders of magnitude (10^4-10^6 yr), providing a time frame for the fluvial-palustrine-lacustrine sediment accumulation in the CE and for sand supply into the central Kalahari. Mineralogical and textural inspections of the sediment are used to characterize the depositional environments and sediment sources. Finally, the data are combined to form a conceptual model of landscape evolution during the early stages of continental rifting.

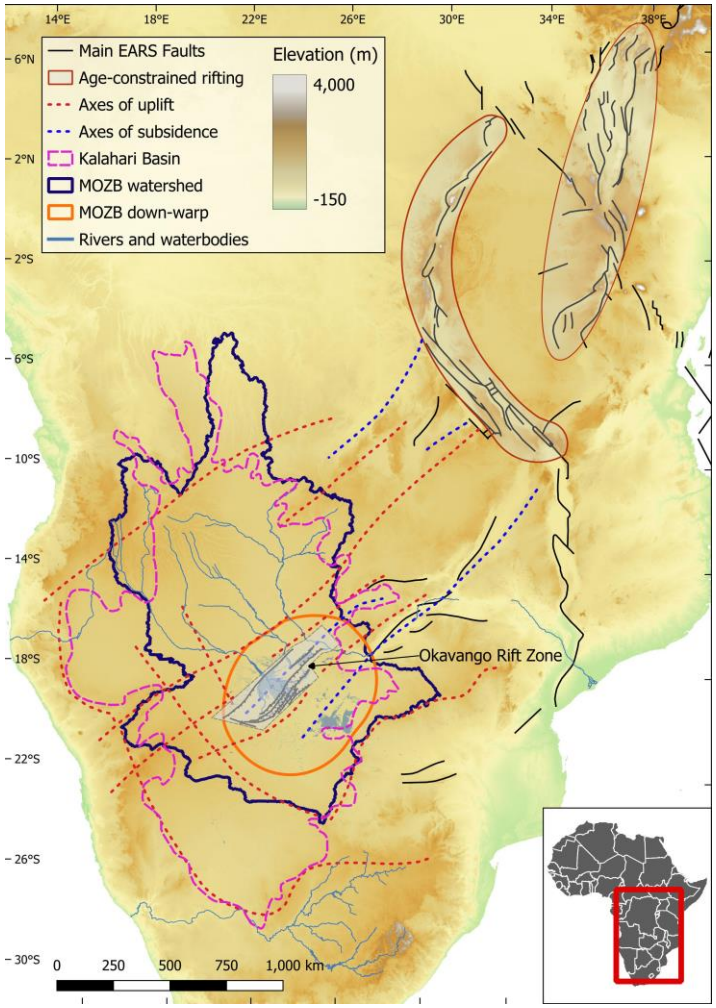

Figure 1. Structural elements in southern Africa including the East African Rift Fault System (Chorowicz, 2005), areas where rifting is chronologically constrained (Michon et al., 2022), and intracratonic structural axes that have been operated since the Neogene (Haddon and McCarthy, 2005). The shaded area indicates the Okavango Rift Zone (Bäumle et al., 2019). The background is an SRTM 30-sec DEM (Farr et al., 2007). Inset denotes the extent of the map on the African continent with its political boundaries.

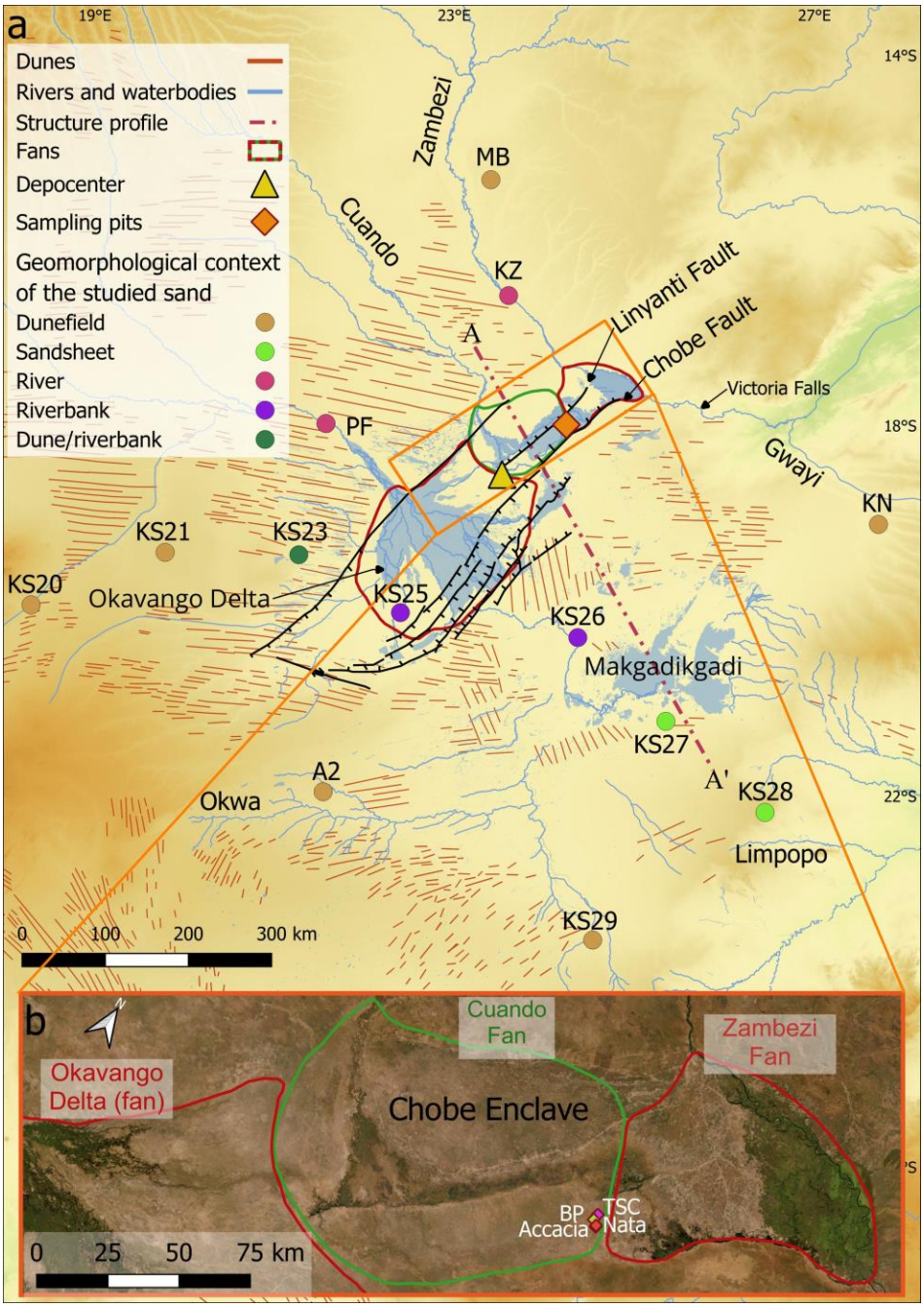

Figure 2. (a) Geomorphology of the Makgadikgadi–Okavango–Zambezi Basin including sand dunes (Thomas and Shaw, 1991), faults (Kinabo et al., 2008; Pastier et al., 2017), hydrogeological features (OpenStreetMap.org; MapCruzin.com), and the alluvial fans of the Okavango Rift Zone (Wilkinson, 2023). The background is an SRTM 30-sec DEM (Farr et al., 2007) (b) Satellite image of the Chobe enclave (ESRI, 2023) and locations of sampling pits.

2. Regional background

2.1. Structural Geology

The CE is situated between the Congo and Kalahari cratons, overlying extensional and accretional structures of Proterozoic and Mesozoic age (Dixey, 1956; Doucouré and de

Wit, 2003; Oriolo and Becker, 2018). It is bounded by elevated structural arches (Figure 2a; Gumbricht et al., 2001), and comprises one out of two syntectonic depocenters in the ORZ. It forms part of the Makgadikgadi–Okavango–Zambezi Basin (MOZB), considered as the southwestern-most segment of the EARS (Fairhead and Girdler, 1969; Reeves, 1972; Kinabo et al., 2008). Several tectonic mechanisms were attributed to the sagging of the MOZB including extension resulting from the advancement of the EARS (Modisi et al., 2000; Wright, 2021) inter-cratonic strains causing lithospheric stretching (Pastier et al., 2017; Yu et al., 2017), as well as Internal and peripheral epeirogenic deformation of the Kalahari Basin (Moore, 1999; Vainer et al., 2021; Mokatse et al., 2022a).

The structural trough of the ORZ is controlled by NE-SW normal to dextral strike-slip faults forming half-graben structures (Figure 4; Modisi et al., 2000; Kinabo et al., 2007; Kinabo et al., 2008) that accommodate an endorheic hydrological system (Figure 2a). This system contains sediments that were transported into the basin, and then recycled, weathered, and eventually diagenetically altered or cemented by secondary minerals (Huntsman-Mapila et al., 2005; Vainer et al., 2021; Garzanti et al., 2022; Mokatse et al., 2023). A major change in the organization of fluvial systems is assumed to have occurred in the early Pleistocene when the upper part of the Zambezi River was captured by its middle part, diverting flow from the terminal basin into the lower base level of the Indian Ocean (Moore et al., 2012; Vainer et al., 2021). Today, the Okavango Basin is occupied by divide fans that are characterized by hydrological links with neighboring basins (Wilkinson et al., 2023). Within the Okavango Basin, a series of tectonically generated reorganizations of the fluvio-lacustrine system occurred throughout the Quaternary (Moore et al., 2007, Schmidt et al., 2023). These events resulted in the deposition of mixed alluvial, fluvial, palustrine, and evaporite sediments, surrounded by eolian deposits on the elevated basin margins.

2.2. Chronostratigraphy

Cenozoic fluvio-lacustrine and eolian sediments (Kalahari Group) up to 300 m-thick fill the MOZB (Haddon and McCarthy, 2005; Podgorski et al., 2013) that was established to form a similar configuration as today around 2.5 Ma (Du Toit, 1933; Day et al., 2009; Cotterill & De Wit, 2011; Vainer et al., 2021). However, a differential structural geometry probably already existed during the Pliocene (Vainer et al., 2021) comprising three sub-basins at the sub-surface, with the thickest depocenter located between the Okavango and Linyanti-Chobe (Figure 3). Basement rocks, mostly Proterozoic volcanic and metasedimentary rocks, as well as Mesozoic metasediments of the Karoo Supergroup and Lower Jurassic basalts (Modisi, 2000) are rarely exposed in marginal and deformed areas within the MOZB (Figure 4). The lithology and composition of the Kalahari Group within the MOZB are known from limited boreholes mainly drilled in the Okavango sub-basin. They reveal the prevalence of sand derived from both local and distant, mostly northerly, source areas, with variable proportions of silt, clay, and carbonates that underwent in places a high degree of chemical weathering (Huntsman-Mapila et al., 2005; Vainer et al., 2021).

The only numeric ages for the earliest deposition in the MOZB are derived from cosmogenic nuclide-based burial dating of two depth profiles in the western Okavango Basin. Ages are 3.06

$^{+4.4}/_{-0.46}$ Ma at the base of the upthrown block and 3.35 $^{+0.39}/_{-0.26}$ Ma in the downthrown block, where basal strata were undatable. The uppermost consolidated sediments at these upthrown and downthrown sites were buried at $1.12^{+0.13}/_{-0.12}$ and 1.34 $^{+0.16}/_{-0.14}$ Ma, respectively. These capping ages were suggested to represent the onset of eolian dominance for sand transport and deposition (Vainer et al., 2021).

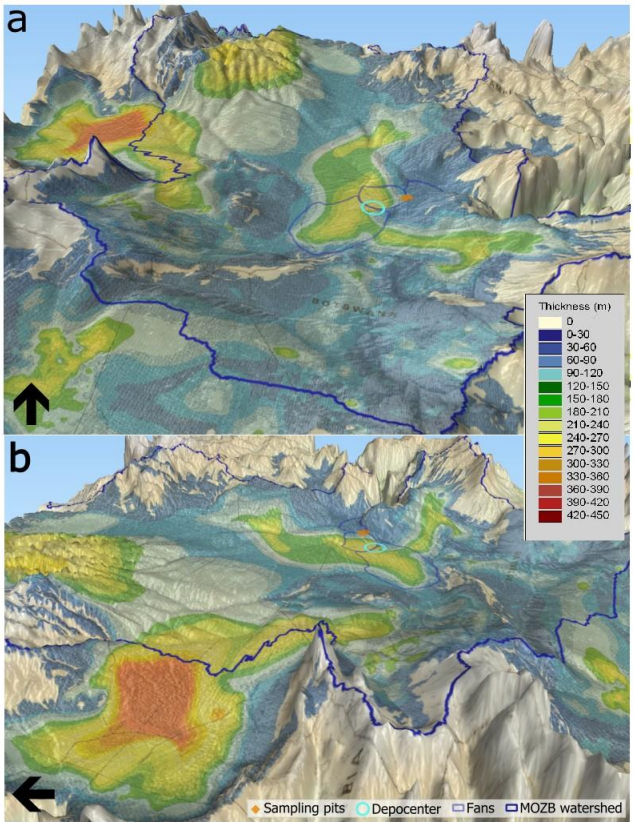

Figure 3. Isopach map of the estimated Cenozoic sedimentation (Kalahari Group) (Haddon and McCarthy, 2005) overlaying 3D elevation model constructed from SRTM version 3.0 Global 1 arc second (Farr et al., 2007) (not to scale). The blue outline marks the MOZB watershed (a) looking northward. (b) Looking eastward.

The surficial fluvio-lacustrine features of the MOZB represent several depositional phases, resulting from changes in fluvial configuration and deposition on top of older alluvium (Thomas and Shaw, 1991). Various materials collected mostly from ridges and pan floors were dated by applying luminescence and ^{14}C dating techniques and were interpreted to represent alternating wet and dry stages (Burrough et al., 2007; Burrough and Thomas, 2013). Earliest ages, as old as 280 ka, were evoked from a limited number of samples (n=3) in these studies, leaving a noticeable age gap with the ~1.1 Ma burial ages at the western MOZB. Successive lacustrine highstands were inferred to occur between 131 ± 11 and 92 ± 2 ka, with another phase centered around 64 ka, and fluctuating conditions between 40 ka and the present. The period between 115 and 95 ka coincides with eolian accumulation in dunes at the northeastern MOZB (Stokes et al., 1998) and the younger inferred highstand stages are coeval with dune buildup in northwestern MOZB areas (Thomas et al., 2000). Within the CE, ages of depth profiles in elevated ridges range between 23.4 ± 1.6 and 1.9 ± 0.3 ka (Burrough and Thomas, 2008; Mokatse et al., 2022), while quartz in carbonate rocks was dated at 48.2 ± 9.6 ka and buried floodplain sands to ~50 ka

(Diaz et al., 2019). Combined, these ages indicate a dynamic hydrogeological fluvio-lacustrine environment at least since ~280 Ka.

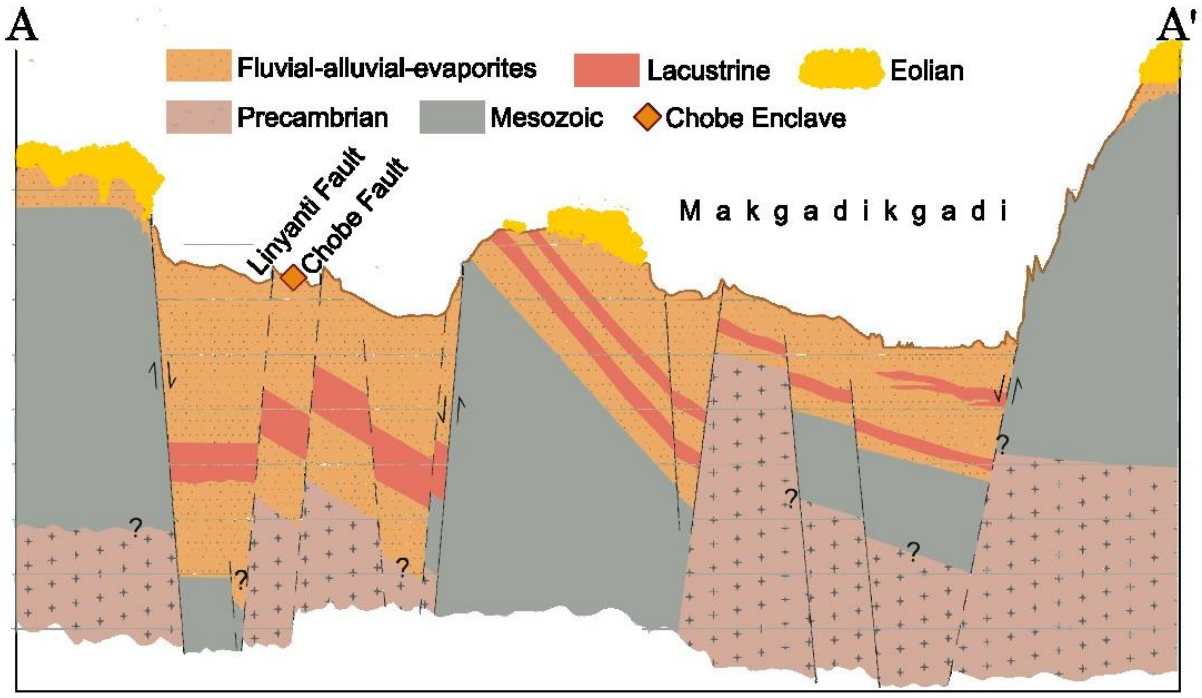

Figure 4. Surface topography (vertical exaggeration ≈ 500) and conceptual geological cross-section (not to scale) through the Makgadikgadi–Okavango–Zambezi Basin (after Bäumle et al., 2019). The horizontal axis corresponds to the magenta/red, semi-dashed line in Figures 2a and 6a, respectively.

3. **Sampling, sample preparation, and analyses**

3.1 Optically stimulated luminescence (OSL) dating

Four pits were excavated to depths of 8-10 m between the Chobe and Linyanti faults within the Cuando alluvial fan. From north to south, they are termed TSC, BP, Nata, and Accacia (Figure 2b). Sampling was made via light-sealed tubes hammered into pit walls or by auger downwards from the bottom of the pit for the deepest samples. Additionally, 1-3 surficial quartz-containing carbonate samples from each site were sampled to constrain the timing of diagenetic processes (i.e. carbonate cementation). These carbonate samples were then cut under subdued red lighting to remove any material that was exposed to light and the remaining inner, un-exposed parts were further treated for analyses.

Organic matter and carbonate precipitates were removed from the 180-212 µm size fraction of all samples with H_2O_2 and 10% HCl, respectively. Using dense-liquid (sodium polytungstate) separation, the fraction between 2.62 and 2.70 g cm^{-3} was etched for 40 min with 40% HF acid to purify the quartz separates and remove the outer layer affected by alpha-radiation. Subsequently, the samples were treated with 10% HCl for >1 h for dissolution of potential Ca-fluoride precipitates (Diza et al., 2016).

The equivalent dose (D_e) of quartz samples was determined using a single-aliquot regeneration dose (SAR) protocol, including four regeneration doses, a zero dose and a repeated dose (Murray and Wintle, 2000). Preheat plateau and dose recovery tests were carried out in the temperature range 180–260 °C for three samples from different profiles to identify optimal preheat conditions. Dose response data constructed from the first 0.7 s of the decay curve (corrected for a background estimated from the last 2 s of this curve) were fitted with an exponential plus linear function in the Analyst software (v4.57; Duller, 2015). Further technical details are given in the Supporting Information. Radioelement concentrations (K, Th, U) were quantified by high-resolution γ-ray spectrometry on ground samples with a mass of ~60–80 g that were stored in a sealed container for at least four weeks prior to analysis.

3.2. Cosmogenic nuclides

Thirteen surficial sand samples from river sands and eolian dunes were processed to determine their ^{10}Be and ^{26}Al content. Seven samples were collected from within the MOZB, and six from its periphery (Figure 2a). The sand was sieved, and the 250-850 µm size fraction underwent sample leaching by aqua regia solution, magnetic separation, and sequential HF + HNO_3 etching (Kohl and Nishiizumi, 1992). Major elements were measured with inductively coupled plasma optical emission spectrometry to verify low concentrations of elements such as Al or Ti. Following spiking and ion-exchange chromatography, isotopic ratios of oxidized targets were measured by accelerator mass spectrometry at Centre de Recherche et d'Enseignement des Géosciences de l'Environnement (CEREGE), France. Isotopic ratios of the in-house standards used for measurements were $7.40*10^{-12}$ and $1.91*10^{-11}$ for $^{26}Al/^{27}Al$ and $^{10}Be/^{9}Be$, respectively. Procedural blank values were in the range between $8.6*10^{-16}$ and $1.66*10^{-15}$ for $^{26}Al/^{27}Al$ and between $2.68*10^{-16}$ and $6.97*10^{-15}$ for $^{10}Be/^{9}Be$.

3.3. Heavy minerals

Two samples from the base of each pit were analyzed for their heavy-mineral assemblage to detect the relative sediment contribution from the Cuando and Zambezi rivers. Heavy minerals were separated by centrifuging in sodium polytungstate (density ~2.90 g cm^{-3}) and recovered by partial freezing with liquid nitrogen. More than 200 transparent heavy-mineral grains were point-counted on grain mounts at suitable regular spacing under the petrographic microscope to minimize the bias caused by grain counting (Garzanti and Andò, 2019). Grains of uncertain identification were checked with Raman spectroscopy (Andò and Garzanti, 2014). Based on the percentage of transparent heavy minerals (tHM), tHM suites are defined as "extremely poor" (tHMC < 0.1) and "very poor" (tHMC 0.1-0.5; Garzanti and Andò, 2007). The ZTR index is the sum of zircon, tourmaline, and rutile over total tHM (Hubert, 1962) and is classically used to estimate sediment "durability" (i.e., the extent of recycling; Garzanti, 2017).

4. Modelling

4.1. OSL dating

Due to the low radioactivity of the sand (Supporting information, Table S1), the cosmic dose rate makes up a significant contribution to the total dose rate (~25–65%, depending on the sample). Therefore, an assessment of the time-dependent cosmic dose rate has been made (Supporting information, Figure S1). This has been estimated step by step by first accounting for the youngest samples taken from the carbonate unit, and hereafter calculating the cosmic dose rates of the samples taken from the sand unit below the carbonate layers, considering the age of the younger samples. Also, carbonate precipitation that can influence the dose rate calculation was considered (Supporting information, Table S2).

Two models were considered for carbonate units (Supporting information, Table S2). One assumes a short time between sand accumulation, carbonate precipitation, and pore filling, thus no modelling of carbonate emplacement over time and its influence on dose rate evolution is carried out (cf. Nathan and Mauz, 2008; Mauz and Hoffmann, 2014; Kreutzer et al., 2019). In case this assumption does not apply, the alternative approach was to perform sensitivity tests by contrasting the conventional OSL ages with those resulting from modelling the time-dependent dose rate using the RCarb model (Mauz and Hoffmann, 2014; Kreutzer et al., 2019). Also, the possibility of U uptake during carbonate precipitation was considered, but given that ^{226}Ra and daughter nuclides contribute >70% of the total β- and γ-dose rate it was concluded that modelling the time-dependent dose rate with reference to poorly constrained assumptions would probably not result in substantially changed ages, necessitating a revision of the environmental interpretation (Degering and Degering, 2020).

The age information obtained for the samples from the carbonate units was considered for estimating the cosmic dose rate applicable to the samples extracted from the sand units below. This approach of individually modelling the cosmic dose rate for each sample based on age information from stratigraphically younger samples was contrasted with the simple (and more common) approach of assuming a constant sedimentation rate (Supporting information, Table S3). This comparison reveals that the age estimates in both ways are indistinguishable at the 1σ confidence level. Therefore, the ages derived from a constant sedimentation rate are used as the

TSC profile shows an almost linear increase in age with depth and because adopting one criterion consistently across the entire profile is simpler and more straightforward whenever age inversions occur.

Another factor causing potential OSL age inaccuracy is the internal dose rate of quartz grains. Especially in low-dose-rate environments, such as the CE, the contribution from the internal dose rate to the total dose rate can be significant. There are only a few previous studies on measured values of internal radioelement concentrations of quartz, and these yielded variable results (e.g., Vandenberghe et al., 2008; Steup, 2015). As the U and Th content of quartz seems to scatter to a much larger extent than, e.g., the K content of K-feldspar, it may not seem reasonable to assume a universal value for the internal quartz dose rate. Within the scope of this study, it was not possible to quantify the internal dose rate of the samples. A previous publication including OSL ages of comparable samples from the Okavango Basin does not report analytical values for the internal quartz dose rate but states that this dose rate contribution does not change the interpretation of the results (Burrough et al., 2009). Thus, zero internal quartz dose rate was assumed, with the implication that age estimates might be younger, should there be a significantly large internal dose rate from quartz grains.

The D_e used to estimate the burial age was derived from applying the Central Age Model (CAM; Galbraith et al., 1999). Ages were calculated with the DRAC software (v1.2; Durcan et al., 2015).

4.2. Surficial residence time

The surficial residence time of the sand was assessed through numerical modelling simulating the accumulation of cosmogenic nuclides under eolian, fluvial, or lacustrine settings by applying the Cosmolian model (Vainer et al., 2018a; Vainer and Ben Dor, 2021; Vainer et al., 2022). Simulations commence with the build-up of cosmogenic nuclides during erosion of source areas that are represented by the coordinates of the headwater of the sample specific-sub basin (Table S4, Supporting Information). Values of 3, 9, and 20 m Ma^{-1} were considered, following Regard et al. (2016) and references therein for erosion rates in the source areas of the sand (Garzanti et al., 2022). Simulations then reproduce the vertical component of sand grains during transport by randomly changing the overburden by 20 cm increments, with twenty-four combinations of possibilities of boundary conditions. The average latitude and altitude values of each sub-basin of a sample define the parameters for cosmogenic nuclides' production rates during transport and are changing only as a function of changing depth. Three amplitudes of 1, 10, and 25 m are used as different boundary conditions to encompass the range of dune heights (Lancaster, 1981; Stokes et al., 1998), and shallow waterbodies in the MOZB (Moore et al., 2012). The retention time at each depth increment is based on a probability function, constructed from dated eolian (Lancaster et al., 2016 and references therein), lacustrine (Huntsman-Mapila et al., 2006; Burrough and Thomas, 2008; Burrough and Thomas, 2013), fluvial (Shaw et al., 1992; Brook et al., 2008), and pluvial (Nash et al., 1981) sediments. Two datasets were constructed to form two probability functions by dividing the OSL/TL/^{14}C ages of buried sediments with the corresponding depth of each dated sample. This conversion from age to vertical displacement rates was applied to 54 eolian samples and 35 fluvial, lacustrine, and palustrine (FLP) samples.

These two datasets were further modified to account for the possible bias stemming from oversampling shallow deposits by removing the fastest 10% from each dataset.

Each simulation during which the build-up of cosmogenic nuclides occurred lasted for 5 My and was repeated with the same conditions 10,000 times. The duration of various successful simulations in which convergence between the simulated and measured concentrations of both ^{26}Al and ^{10}Be occurred have been summarized and are interpreted as the most probable timing since the modelled sand was introduced into the landscape (Vainer et al., 2022).

5. Results

5.1 OSL dating

The results of D_e estimates are shown in Table S1 in Supporting Information and calculated ages are shown in Table 1 and illustrated in Figure 5. The assumption that the ^{238}U decay chain is in secular equilibrium was followed for samples that were taken from carbonate-cemented units. Ages of 29 ± 3 ka and 81 ± 7 ka for samples TSC 0.8 and TSC 2.0 were obtained, respectively. Samples NATA 0.8 and NATA 0.8B, taken from the same depth of 0.8 m, yielded ages of 74 ± 7 ka and 58 ± 6 ka, respectively, not overlapping at the 1σ confidence level. A sample taken 1.2 m below (NATA 2.0), however, produced an age of 64 ± 6 ka, consistent with the dating results of both overlying samples and with and age of 55 ± 6 ka obtained at 0.6m depth by Mokatse et al., 2022a. At the ACA site, the sample from 0.8 m depth yielded an age of 54 ± 5 ka, and the deepest carbonate bed at 4.6 m depth is dated to 163 ± 16 ka, which is synchronous (within uncertainty) with the deposition of the sand at 5.8 m depth at 137 ± 11.

Table 1. Dose rate assessment and age calculation. A value of 10 ± 3 wt% water was assigned to all samples expect from waterlogged samples where 21 ± 3 wt% values were assigned. The cosmic dose rate of the sand samples (below the carbonate layers) was modelled according to the thickness of sand and carbonate units and the time of emplacement of overlying layers. See Supporting Information for further details.

Sample	Generalized content	U [ppm]	Th [ppm]	K [%]	Cosmic $\dot{D}$ [Gy ka^{-1}]	Total $\dot{D}$ [Gy ka^{-1}]	CAM De [Gy]	Age [ka]
ACA 0.8	Carbonate + sand	0.35 ± 0.09	0.29 ± 0.18	0.045 ± 0.005	0.219 ± 0.020	0.348 ± 0.027	18.71 ± 0.82	54 ± 5
ACA 4.6	Carbonate + sand	0.83 ± 0.22	1.08 ± 0.33	0.100 ± 0.014	0.159 ± 0.016	0.482 ± 0.040	78.51 ± 4.44	163 ± 16
ACA 5.8	Sand	0.85 ± 0.10	1.59 ± 0.09	0.158 ± 0.021	0.142 ± 0.014	0.551 ± 0.027	75.27 ± 4.77	137 ± 11
ACA 6.3	Sand	0.80 ± 0.11	1.53 ± 0.28	0.088 ± 0.013	0.138 ± 0.014	0.472 ± 0.027	71.92 ± 4.04	152 ± 12
ACA 7.0	Waterlogged sand	0.50 ± 0.10	0.93 ± 0.12	0.049 ± 0.009	0.133 ± 0.013	0.314 ± 0.020	25.46 ± 1.46	81 ± 7
BP 5.5	Sand	0.44 ± 0.12	0.80 ± 0.12	0.116 ± 0.016	0.142 ± 0.014	0.383 ± 0.026	57.21 ± 2.53	150 ± 12
BP 6.2	Sand	0.36 ± 0.13	0.47 ± 0.19	0.061 ± 0.009	0.136 ± 0.014	0.292 ± 0.026	51.32 ± 3.58	150 ± 16
BP 6.8	Sand	0.34 ±	0.49 ±	0.053 ±	0.132 ± 0.013	0.278 ± 0.023	43.86 ±	201 ± 20

		0.11	0.15	0.008			2.40	
BP 8.3	Sand	0.16 ± 0.08	0.31 ± 0.12	0.019 ± 0.004	0.122 ± 0.012	0.190 ± 0.018	55.99 ± 3.39	252 ± 27
BP 10	Waterlogged sand	0.71 ± 0.06	1.34 ± 0.18	0.094 ± 0.012	0.112 ± 0.011	0.389 ± 0.018	47.87 ± 2.42	203 ± 14
NATA 0.8	Carbonate + sand	0.22 ± 0.10	0.16 ± 0.27	0.052 ± 0.006	0.212 ± 0.021	0.312 ± 0.029	78.87 ± 3.99	74 ± 7
NATA 0.8 B	Carbonate + sand	0.36 ± 0.11	0.07 ± 0.26	0.055 ± 0.010	0.212 ± 0.021	0.338 ± 0.030	23.14 ± 0.87	58 ± 6
NATA 2.0	Carbonate + sand	0.51 ± 0.12	0.34 ± 0.08	0.050 ± 0.008	0.191 ± 0.019	0.360 ± 0.027	19.49 ± 0.87	64 ± 6
NATA 3.5	Sand	0.31 ± 0.07	0.95 ± 0.16	0.095 ± 0.015	0.171 ± 0.017	0.376 ± 0.024	23.05 ± 0.99	143 ± 11
NATA 4.5	Waterlogged sand	0.31 ± 0.10	0.78 ± 0.02	0.048 ± 0.007	0.161 ± 0.016	0.298 ± 0.021	53.74 ± 2.46	180 ± 16
NATA 5.0	Waterlogged sand	0.35 ± 0.10	0.48 ± 0.26	0.036 ± 0.006	0.157 ± 0.016	0.275 ± 0.023	53.53 ± 2.77	94 ± 10
TSC 0.8	Carbonate + sand	0.52 ± 0.09	0.54 ± 0.26	0.099 ± 0.017	0.212 ± 0.021	0.438 ± 0.029	25.81 ± 1.43	29 ± 3
TSC 2.0	Carbonate + sand	0.58 ± 0.14	0.40 ± 0.27	0.062 ± 0.010	0.191 ± 0.019	0.388 ± 0.032	12.55 ± 0.79	81 ± 7
TSC 3.1	Sand	0.69 ± 0.11	1.44 ± 0.10	0.136 ± 0.021	0.176 ± 0.018	0.524 ± 0.029	31.49 ± 1.31	116 ± 9
TSC 4.0	Sand	0.23 ± 0.09	0.56 ± 0.17	0.036 ± 0.006	0.166 ± 0.017	0.279 ± 0.023	60.89 ± 3.19	139 ± 14
TSC 6.0	Sand	0.27 ± 0.11	0.58 ± 0.12	0.029 ± 0.005	0.149 ± 0.015	0.265 ± 0.023	38.76 ± 2.30	199 ± 19

The ages of sand that underlie the carbonate layers were calculated assuming cosmic dose rate production during constant sedimentation rate and range between 252 ± 27 and 116 ± 9 ka (Table 1). Ages generally follow a stratigraphic order, apart from samples ACA 7.0, BP 10, and NATA 5.0. These outliers were saturated in water when sampled (discussed in Supporting Information).

5.2 Cosmogenic nuclides

Blank corrected concentrations of ^{26}Al and ^{10}Be of sand samples range from 1.18×10^6 to 14.03×10^6, and from 0.33×10^6 to 3.67×10^6 atoms g^{-1}, respectively (Table 2). Although distributed over a noticeable concentration range, $^{26}Al/^{10}Be$ ratios are clustered in a narrow spectrum between 3.5 and 4.7, not correlated with nuclides' concentrations, which are not correlated in turn with distance from the CE.

Kernel density estimates resulting from the Cosmolian model produce overall log-normal distributions and their weighted average value reflects the most probable surface residence time of each sand sample (Figure 6). While the different combinations of scenarios generally converge into a distinct peak, several samples present a bi-modal distribution with a relatively narrow combined range or positive skewness. These are probably the outcome of grains within the same sample with different sources and transportation histories (Vainer and Ben Dor, 2021), and this variance is reflected in the uncertainty estimation.

Residence time estimates for all analyzed samples span the time range between $0.91^{+0.24}/_{-0.22}$ and $2.22^{+0.96}/_{-0.69}$ Myr (Table 2). Their ages display a correlation (with r = 0.57) with distance from

the CE, with ages being overall younger with proximity to the depocenter on the western margins of the CE (Figure 6). Simulations that were carried out with an overburden of 1 m (density of 1.7 g cm^{-3}) did not reach convergence with the measured values. This result agrees with the evoked mean value of the overburden required for simulations to converge with measured concentrations. This value is 4.7 ± 3.9 m if all samples are considered, or 5.0 ± 3.3 m if the two thinnest and two thickest simulated values of overburden are excluded (Table 2). Furthermore, the least likely assigned erosion rate during production in source areas is 3 m Ma^{-1}, in accordance with major sources in northern provinces where erosion rates are higher (Regard et al., 2016; Garzanti et al., 2022).

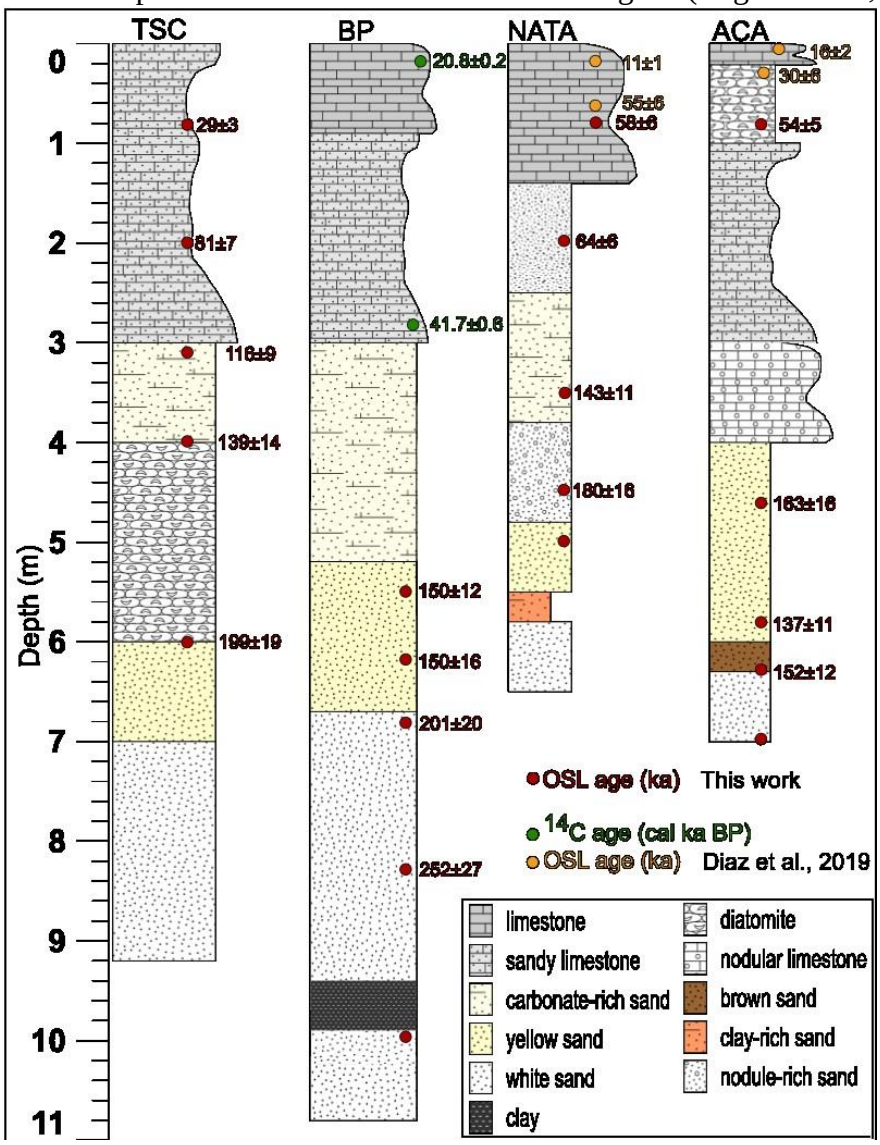

Figure 5. Columnar sections and chronology of deposits recovered from sampling pits dug in the Chobe Enclave. Red circles with no age specification indicate water-logged samples where estimated ages are out of stratigraphic order. The locations of pits are shown in Figure 2b.

5.3 Mineralogy

All analyzed sands are pure quartzose, with quartz representing 98-100% of the grain framework, with a few feldspars (almost exclusively K-feldspar) and rare mica. The very poor to

extremely poor tHM suite consists mainly of tourmaline, associated with kyanite, zircon, and staurolite (Table 3). Rutile, epidote, titanite, hornblende, anatase, and brookite, are minor, sillimanite sporadic, and garnet and apatite are rare. The mineralogical suite significantly differs (e.g., has much more kyanite; Table 3) from the assemblage that characterizes the regional Kalahari sand dunes. The ZTR index is 58±10, and the staurolite/kyanite ratio ranges between 0.4 and 1.2. Simple forward mixing calculations (Garzanti et al., 2012) and similarity analysis (Vezzoli and Garzanti, 2009) suggest subequal contributions from the Cuando and Uppermost Zambezi.

Table 2. Cosmogenic nuclides concentrations of sand samples from the Okavango Rift Zone (ORZ) and its vicinity and their simulated results given by the Cosmolian Model. The results shown include (1) the most probable average overburden (2) the ratio of successful simulations of vertical quartz grain displacement rates evoked from using fluvial, lacustrine, and palustrine (FLP) datasets for simulating vertical displacement rates vs. those from eolian datasets, and (3) the surficial residence time that represents the most probable time since the sediment was introduced into the landscape. Parameters used as input are detailed in Table S4, Supporting Information.

Sample	Current landform	Elevation [m]	$^{26}Al \times 10^{6}$ [at g^{-1}]	$^{10}Be \times 10^{6}$ [at g^{-1}]	$^{26}Al/^{10}Be$	Simulated overburden height [m]	Residence time [Myr]
PF	River	1016	1.44±0.18	0.34±0.01	4.2	7.4	$1.27^{+0.43}/_{-0.32}$
A2	Dunefield	1127	3.93±0.18	1.03±0.04	3.8	4.5	$1.43^{+0.34}/_{-0.25}$
KN	Dunefield	1064	2.63±0.14	0.70±0.02	3.7	5.2	$1.53^{+0.32}/_{-0.27}$
MB	Dunefield	1072	1.18±0.15	0.33±0.02	3.5	7.1	$2.22^{+0.96}/_{-0.69}$
KZ	River	977	3.14±0.19	0.68±0.02	4.6	4.8	$0.98^{+0.25}/_{-0.26}$
KS20	Dunefield	1250	12.9±0.58	3.67±0.11	3.5	2.4	$2.17^{+1.02}/_{-0.42}$
KS21	Dunefield	1217	3.0±0.15	0.77±0.03	3.9	5.6	$1.39^{+1.48}/_{-0.24}$
KS23	Dune/river bank	1027	5.48±0.25	1.31±0.05	4.2	4.1	$1.14^{+0.39}/_{-0.25}$
KS25	Riverbank	941	2.75±0.14	0.62±0.02	4.5	5.4	$1.04^{+0.24}/_{-0.22}$
KS26	Riverbank	931	4.23±0.20	0.90±0.03	4.7	4.2	$0.91^{+0.24}/_{-0.22}$
KS27	Sandsheet	962	14.03±0.61	3.28±0.10	4.3	2.0	$1.59^{+0.8}/_{-0.37}$
KS28	Sandsheet	1249	4.38±0.20	1.18±0.05	3.7	4.3	$1.46^{+0.35}/_{-0.26}$
KS29	Dunefield	1058	3.80±0.19	0.93±0.04	4.1	4.6	$1.27^{+0.81}/_{-0.24}$

Table 3. Heavy mineral assemblages. Data of regional fluvial and eolian sand are after Garzanti et al. (2021) and (2022), respectively.

Sample	HMC w%	tHMC w%	zircon	tourmaline	rutile	Ti Oxides	titanite	apatite	epidote	garnet	staurolite	andalusite	kyanite	sillimanite	amphibole	clinopyroxene	others	ZTR	St/Ky

TSC6.0	0.08	0.05	8	43	7	0	0	0	5	0	20	0	17	0	0	0	0	58	1.2
TSC6.8	0.10	0.06	17	35	4	0	0	0	2	0	19	0	21	1	0	0	0	56	0.9
BP5.5	0.83	0.47	17	32	7	0	0	0	6	0	13	0	24	0	0	0	0	57	0.5
BP10.0	0.22	0.13	12	33	3	2	5	0	4	0	10	0	29	0	0	0	0	48	0.4
ACA6.3	0.13	0.08	14	38	4	0	1	0	4	0	11	0	25	0	2	0	0	55	0.5
ACA7.0	0.19	0.09	17	37	7	0	2	0	5	0	13	0	22	0	1	0	0	60	0.6
NATA3.5	0.19	0.11	17	40	6	0	3	0	2	0	13	0	16	0	0	0	2	63	0.8
NATA5.0	0.21	0.11	18	41	10	0	0	1	6	1	9	0	16	0	1	0	0	68	0.6
										Fluvial sand									
Cuando	0.07	0.03	24	27	6	0	1	0	4	0	19	1	11	0	5	0	0	57	1.8
Linyanti	0.10	0.06	9	51	6	0	0	0	0	0	20	1	13	0	0	0	0	66	1.5
Chobe	0.27	0.14	29	24	6	0	0	0	5	0	10	0	23	0	2	0	0	69	0.4
Zambezi (Kazungula)	0.39	0.25	22	15	6	0	0	0	8	1	7	0	36	1	3	0	0	43	0.2
Zambezi (Livingstone)	0.52	0.23	18	16	5	2	0	1	12	0	4	1	27	0	4	14	0	39	0.1
Zambazi (Sheshka)	0.2	0.1	12	18	14.0	0	1	0.5	9	0	8	1	21	0.5	2	12	0	44	0.4
Zambezi (Kazungo)	0.2	0.1	24	25	8	0.5	0	0	3	0.5	7	0	30	0.5	1	0	0	57	0.2
										Kalahari Sand Dunes									
KS27	0.3	0.3	33	18	7	0	0.5	0.5	28	5	2	0	1	0	1	6	0	58	1.5
KS28	0.5	0.1	47	34	5.5	0	0.5	0.5	0.5	0	10	0	1	0	0	1	0	87	10.5
KS29	0.3	0.1	40	43	5.0	0	0	0	1	0.5	8	0	2	0	0	1	0	88	4.5
A2	0.2	0.2	8	37	1	0	0	0	1	0	43	0	8	0	3	0	0	46	5.4
KS30	0.6	0.3	36	15	6	0	0.5	0	40	1	0.5	0	1	0	0	0	0	57	0.3

6. Discussion

6.1 Deposits of the Cuando-Zambezi alluvial fans

The studied pits are spread over an area smaller than 5 km^2 (Figure 2b), and their sedimentary sequences display spatio-temporal variations described below and illustrated in Figure 5.

(1) The basal sediments from all four pits comprise regionally continuous white sand, intercalated by muds with a phyllosilicate content ranging between 13-35% (Mokatse et al., 2023). The occurrence of > 70% clay sub-unit (most of which is a mixture of kaolinite and sepiolite) within the white sand at BP (Figure S8, Supporting Information) confirms deposition in a composite environment with markedly changing fluvial energy through time, as typical of alluvial fans (Stock, 2013). The ages of the strata above the white sand constrain the oldest deposits as not later than ~200-150 Ka, as also indicated by two OSL ages of the lower sand unit at BP that were buried at 252 ± 27 and 201 ± 20 Ka.

The deepest samples from BP, NATA, and ACA pits were taken from water-logged units using an auger drill and yielded ages out of stratigraphic order. Possible reasons for this age underestimation are discussed in the Supporting Information but this point remains unclear.

Therefore, the earliest deposition at the studied sites is constrained to have occurred before 250 Ka.

(2) Yellow/brown sand overlying the white sand is observed at all sites, displaying some lateral variations and variations in carbonate content. Overall, the clay content in this unit ranges between 19 and 40 %; higher sepiolite abundance at the expense of kaolinite in comparison with the white sand below may imply some evaporitic conditions (Mokatse et al., 2023). The yellow sand facies was deposited between ~200 and 140 ka (199 ± 19 and 137 ± 11 ka; n = 5). At the ACA site, the yellow sand is different in nature than in the other sites as it is noticeably rich in carbonate and iron. This could indicate a reworked paleosol that may explain the age inversion observed at ACA (even though ages overlap within their analytical uncertainty), which could be also explained by bioturbation. At the NATA site, highly siliceous, bioturbated deposits accumulated at 180 ± 16 Ka. Between ~200 and 139 ± 14 Ka, a diatomite unit accumulated at TSC. These observations point to multiple depositional environments with a relatively large range of water depths and depositional energies, composition of solutes, and precipitation-to-evaporation ratios. These sub-environments were found in close proximity inside a dynamic alluvial fan setting.

(3) The diatomite and carbonate deposits that lie in unconformity above the sand below (Figure S8, Supporting Information) mark the initial deposition in a lacustrine environment that took place during the regionally wet MIS 5 (Burrough et al., 2009). Their deposition is constrained by three samples from two sites to have occurred after ~200 ka, with depositional ages of 143 ± 11 and 116 ± 9 Ka. Lateral and vertical calcite content changes (Mokatse et al., 2023), ranging from 0 to 4% at the NATA and TSC sites (where ages were determined), to ~50% at BP and ACA where age is defined only by correlation. The change from primary siliceous deposits that contain no carbonate to the deposition of carbonate implies a noticeable change in the chemistry of the precipitating solution that could have resulted from an adjustment to morphotectonic or climatic shifts, as discussed below.

(4) A change in the environment occurred at 81 ± 7 ka and is synchronous with the global climatic perturbations and regional environmental changes of MIS 3 (e.g. Agostaand and Compagnucci, 2016; Stewart and Jones, 2016). A carbonate-rich palustrine/lacustrine environment is inferred due to the abundance of calcite at all sites, commonly representing the most abundant mineral (Mokatse et al., 2023). The upper units at the NATA and ACA sites, which lie ~0.5 km from each other, are constrained by six OSL ages ranging from 58 ± 6 and 11 ± 1 ka. While carbonate is the main precipitate at NATA around 50 ka, diatomites and clays (with high sepiolite content) were deposited at ACA, pointing to less alkaline conditions locally, possibly related to pluvial lake settings. These sediments resemble surficial deposits of the Okavango Delta that originate from semi-continuous flood events under semi-arid conditions and desiccation. In the Okavango Delta, silicious and carbonate-rich precipitates are discretely deposited, and while carbonate minerals are present, they are far less common in the Okavango Delta than in the CE (McCarthy and Ellery, 1995; Ringrose et al., 2008; Dauteuil et al., 2021). These differences raise the question of the composition and origin of the parent solutions of the water flows in the CE during the later Pleistocene.

6.2 Provenance

The mineralogical assemblages of all buried CE samples imply similar sources, represented by a mixture of sediments presently carried by the Zambezi and Cuando rivers that drain northern terrains (Garzanti et al., 2021). This could be the result of the inter-basin hydrological connectivity with the Zambezi River that changes naturally as drainages are separated or combined through avulsion and due to external forces, such as climate change and tectonic activity (Shaw and Thomas, 1992; Wilkinson et al., 2023). Furthermore, XRD patterns of the studied samples reveal that non-carbonate mud samples (Figure S8, Supporting Information) contain 14-46 % phyllosilicates (Mokatse et al., 2023), congruent with a primary fluvial/alluvial transporting agent. Moreover, kyanite enrichment in sediments carried by the Chobe River (the spill of the Cuando into the CE) across the CE, relative to the upper reaches of the Cuando, points to the incorporation of fluvial sediments from the Upper Zambezi by the Chobe, and their reworking from deposition in alluvial fan settings (Garzanti et al., 2022; Mokatse et al., 2022b). A northern source is also suggested for the surficial sand that is carried by rivers into the MOZB as it presents a significantly higher success rate of Cosmolian simulations by applying displacement rates constructed from the FLP rather than the eolian dataset rates (Table 2). This sand (samples KS25, KS26) has ≤ 2% success in Cosmolian convergence events for scenarios with an erosion rate of 3 m Ma^{-1} that characterizes southern source areas, while higher erosion rates that characterize northern areas yield higher successful scenarios. This pattern of simulations resembles the simulations of northern dune sand and river samples (MB, KZ, PF, KS21) that arrive from areas with higher erosion rates (Garzanti et al., 2022) and differ from the rest of the sand samples to the south that present noticeable convergence also for scenarios with slower eroding source areas (Figure 6). Furthermore, a coupled fluvial-eolian transport agent is deduced also for currently eolian dune samples (Garzanti et al., 2022), as all modelled samples experienced successful simulations by applying rates from both FLP and eolian datasets.

Although some mineralogical similarity exists with sand dunes located on the upper reaches of the Zambezi, the mixed source for the buried CE sediments differs from sources that predominate the Kalahari sand dunes as well as from their diagenetic history (Table 3). Their differences in nature and age are reflected in their colors. The sand in the CE is mostly white and yellow (Figure 5; Supporting Information S8) resulting from secondary iron oxyhydroxides coating, likely due to hydration under alkaline conditions during fluvial transportation. Conversely, the eolian Kalahari Sand is red (Wang et al., 2007) due to longer pedogenesis with rubificataing edaphic conditions (Walker and McKee, 1979). Hence, whereas the modes of the grain size distribution of CE sands and Kalahari sand lie within the same range (Mokatse et al., 2022a), they do not share a genetic link and do not represent re-deposition of Kalahari dunes. Additional observations point to fluvial incision and transport of material from elsewhere that postdates the establishment of the dunes. These observations include (1) the offset and truncation of dunes west of the Okavango Delta by faults and the lowering of base level associated with the subsidence of the MOZB (McFarlane and Eckardt, 2007); and (2) the flow of the Gwayi River parallel to the crests of linear dunes in the eastern MOZB (Figure 2a) (Thomas and Shaw, 1991; Moore et al., 2012). Thus, the reason for the different mineralogical and textural signatures between the Kalahari Sand and the CE buried sediments is probably the subsidence of the CE and the incision of rivers into it (after the fixation of the eolian sand), carrying sediment from their headwaters in a significantly greater proportion than recycled eolian sand from their riverbanks.

6.3 Sand chronology

Eolian sand within the MOZB was exhumed between 2.22 $^{+0.96}/_{-0.69}$ and 1.14 $^{+0.39}/_{-0.25}$ Ma, marking the upper age limit for the last significant geomorphologically evident subsidence event in the CE, as no sand with similar sources and diagenetic history is found in the CE. The distribution of the mean residence times of all sand samples correlates moderately (r = 0.6) with elevation and increases with distance from the Linyanti-Chobe Basin (r = 0.57; Figure 6). Collectively, this points to the preservation of the older sediments on the higher margins of the tectonic trough of the CE and the incorporation of more recently eroded material downwards into the evolving basin.

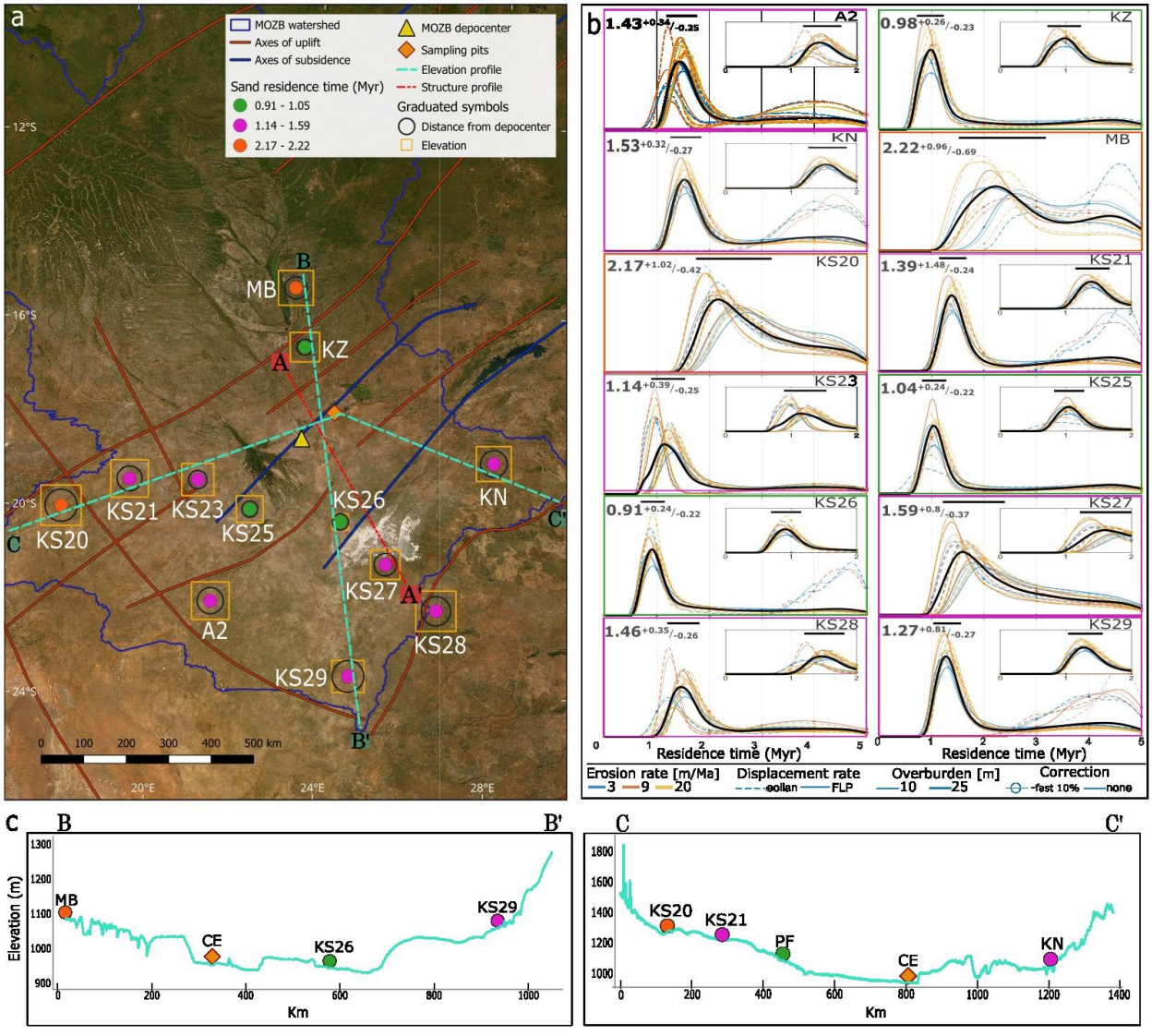

Figure 6. (a) Sands of the Makgadikgadi–Okavango–Zambezi Basin are categorized into three groups based on their sedimentary residence time. Simplified structural axes highlight the multi-block configuration (Haddon and McCarthy, 2005) overlying a satellite image of central southern Africa (ESRI, 2023). The size of the graduated symbols increases with larger values. (b) Kernel density estimates of the sedimentary residence time of sands, simulated with the Cosmolian Model (Vainer et al., 2018; Vainer and Ben Dor, 2021). The probability plots show successful runs in which simulated concentrations of ^{26}Al and ^{10}Be simultaneously matched with their analytical

values. 10,000 iterations were applied for each combination of the boundary conditions. The various scenarios include three values of erosion rate at the source areas, vertical displacement rates constructed from accumulation ages of either eolian or Fluvial-Lacustrine-Pluvial (FLP) datasets, and three values representing different transportation agents that resolve in changeable overburden thickness. The weighted average of the matching simulations is shown with a black solid line with uncertainty marked by the horizontal line on top, calculated with full-width at the half-maximum approach. The simulations performed for the PF sample are not shown due to a <1% success rate. (c) Elevation profiles of two nearly perpendicular cross sections across the basin, passing through the Chobe Enclave, constructed from SRTM 30 sec DEM (Farr et al., 2007).

The Jenks natural breaks optimization highlights three periods of sand introduction that also roughly correspond to their structural position with respect to the CE and their geomorphological context (fluvial/eolian) at present (Figure 6). (1) Sand collected in fluvial settings near the CE depocenter belongs to the youngest age group with mean ages in the range of 1.05-0.91 Ma (n = 3). This excludes additional input from the Okavango River (PF) that yielded less than 1% of successful simulations with a mean age of $1.27\ ^{+0.43}/_{-0.32}$ Ma. In the subsurface of the western MOZB, sediments younger than ~1.1 and 1.4 Ma are not preserved in the downthrown and upthrown blocks, respectively (Vainer et al., 2021). The absence of buried deposits younger than ~1 Ma and the lack of sand production since that time suggest a re-organization affecting the interconnection between the fluvial and eolian systems around 1 Ma. The paucity in sediment burial after ~1 Ma is observed throughout the southern Kalahari, suggesting the beginning of a primary regional eolian phase (excluding the ORZ), following tectonic uplift of the Kalahari margins (Matmon et al., 2015; Vainer et al., 2018b). (2) Eolian sand located on the surface that is just above the CE yielded mean residence time ages of 1.59-1.14 Ma (n = 7). During this period, sand from eolian landforms located ~50-300 km to the south and southwest of the MOZB water divide was extensively formed (Vainer et al., 2022), pointing to a regional (over the MOZB limits) phase of sand production. (3) The most distal to the CE eolian sand was exhumed around 2.2 Ma (n=2; Figure 6). The initial sand supply into the MOZB coincides with the deposition of basal eolian sand characterized by eolian grain size distribution in the southwestern Kalahari between $2.2\ ^{+0.18}/_{-0.17}$ and $1.74\ ^{+0.15}/_{-0.15}$ Ma (Vainer et al., 2022) and with distinct hydrological changes in the western Kalahari at ~2 Ma (Miller et al., 2010). Together, this chronology points to Kalahari Basin-scale changes that resulted in the initiation of sand cover and its eolian distribution around 2.2 Ma.

6.4 Landscape evolution of the Okavango Rift Zone since the Pleistocene

The chronology of landscape evolution in the ORZ is addressed via two dating methods that differ by an order of magnitude in their dating capabilities, allowing temporally constraining the rifting before and after the last significant phase of subsidence in the CE. The chrono-structural development of the ORZ can be tracked through the relatioshipss between sedimentation and geomorphology, hinting at the stages of morphodynamical evolution of the nascent rifting zone (Figures 6, 7). Two elevation profiles that pass through the CE illustrate a symmetric (N-S, E-W) structural-block development during continental rifting (Holz et al., 2017), with the oldest sediments deposited at ~2.2 Ma. The two sites, where sand of this age is present, are located on elevated landforms on the outer-most structural blocks with respect to the CE (Figure 7). These sands could have been generated due to erosion following relief forming in the MOZB by virtue of tectonics at ~2.5 Ma (Thomas and Shaw, 1990; McCarthy et al., 2002; Moore et al., 2012; Vainer et al., 2021). A more recent tectonic activity resulted in the formation of a lower base level, enabling the preservation of older sand on the surface of the elevated landforms.

The inner lower blocks that lie above the CE accommodate sand that was formed at ~1.6-1.1 Ma, representing a second phase in landscape lowering and deformation. Tectonism at ~1.4 Ma was biochronologicaly inferred from the lacustrine radiation of tigerfish in the MOZB (Goodier et al., 2011) and was claimed by Moore et al. (2012) to cause changes in the configuration of the MOZB hydrological system. Such a change is also observed in the chrono-stratigraphy of the sand, as no sand that is found today in eolian settings has been produced since. Therefore, this timing signifies the earliest date for subsidence and formation of accommodation space in the

CE. Finally, the successful modelling efforts of the fluvial sand indicate that it was exhumed around ~1 Ma, pointing to a change in the depositional environments that possibly resulted from a new structural configuration occurring around the same time (Matmon et al., 2015; Vainer et al., 2018b), concurrent with the Middle Pleistocene Transition (MPT, 1.2-0.75 Ma; Herbert, 2023).

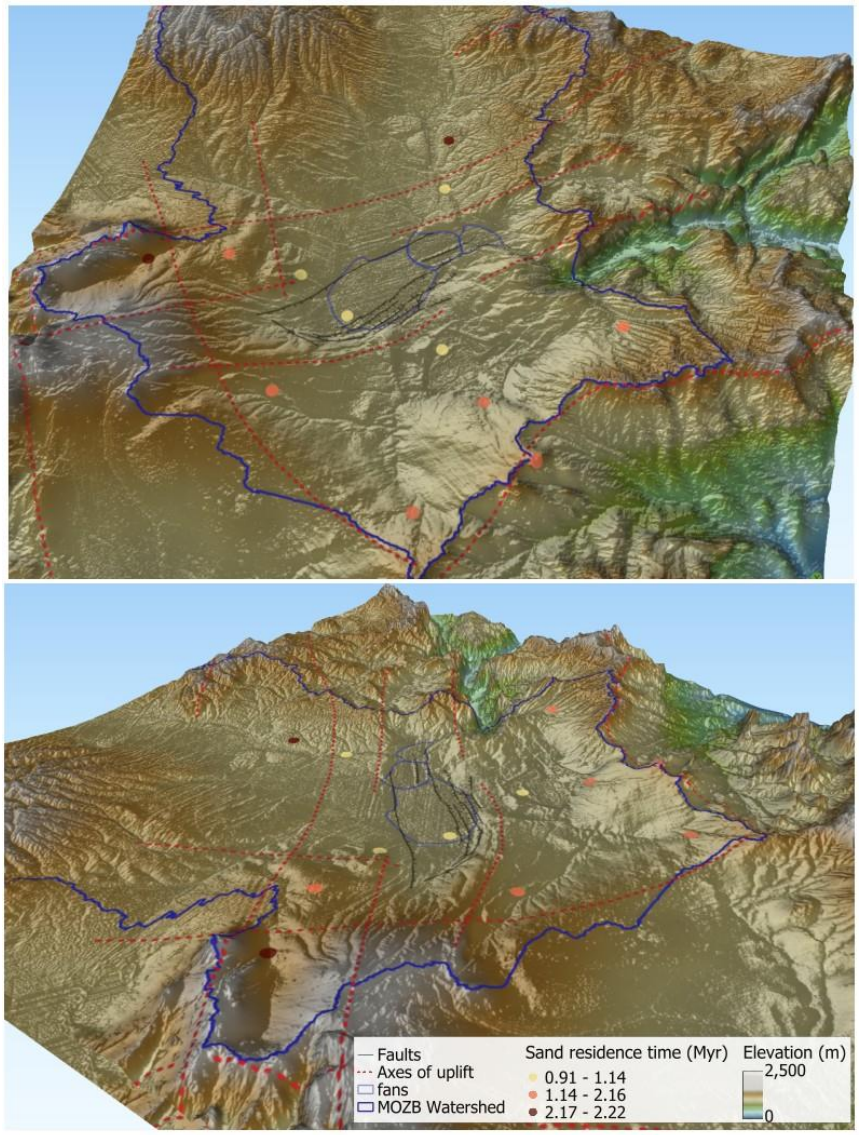

Figure 7. Sand residence time and structural/geomorphological elements on top of a 3D elevation model of the Makgadikgadi–Okavango–Zambezi Basin (purple outline), constructed from SRTM version 3.0 Global 1 arc second DEM and 30 sec DEM (Farr et al., 2007) (not to scale). (a) looking northward. (b) Looking eastward.

Burial ages of basal deposits in the CE could indicate the timing of the last significant rifting stage. However, such deposits were not reached in this work, and thus direct dating of the earliest sedimentation in the CE could not be achieved. We could only determine that accommodation space in the CE was available after 1.1 Ma and before 0.25 Ma. Sedimentary sequences deposited during continental rifting may overlie volcanic or basement rocks and typically consist of gravel, followed, or intercalated by fluvio-deltaic sands, overlain in turn by

lacustrine and evaporitic deposits (Olsen et al., 1996; Young et al., 2000; Nielsen et al., 2007). The syn-rift sequence described in this study lacks basal conglomerate and begins with alluvial sand. In accordance with the isopach map of Haddon and McCarthy (2005; Figure 3), the unreached sedimentary suite below the studied pits in the CE is possibly 20-50 m thick. Assuming similar accumulation rates to those of the dated sediments, and accounting for the estimated missing thickness range, it is speculated that sedimentation in the CE may have started closer to 1 Ma than to 0.25 Ma.

Several observations point to the existence of a topographic depression since ~1 Ma in the MOZB, where waterbodies were sustained and linked to tectonic-induced landscape evolution (Grove, 1969; Moore et al., 2012). (1) Phylogeographic records of catfishes point to their radiation in a lacustrine environment at 0.9 ± 0.5 Ma. (Day et al., 2009; Cotterill and De Wit, 2011) (2) Early Stone Age (ESA) artifacts with a minimum age of 0.5 Ma were found in paleo lacustrine settings (McFarlane and Segadika, 2001; McFarlane and Eckardt, 2006; Moore and Cotterill, 2007) (3) Gravels containing ESA artifacts were found <10 km downstream the Victoria Falls (Figure 2), indicating the initiation of gorge incision due to lacustrine overtop from the MOZB into the Zambezi River at 1.1-0.65 Ma (Clark, 1950; Moore and Cotterill, 2010). The existence of this waterbody (or waterbodies) in the CE cannot be determined with the findings of this study.

The earliest dated waterbody deposits in the CE are diatomite and carbonate which accumulated at ~140 ka (Figure 5). This waterbody could have extended some 300 km to the southwest, where partially cemented lakebed deposits and coarse sand interpreted to represent a beach ridge accumulated at 133 ± 12 and 140 ± 11 ka, respectively (Shaw et al., 2003; Burrough et al., 2007). These sediments were interpreted to have formed under wet environmental conditions, as their deposition is synchronous with cave deposits on the western elevated margins of the MOZB (Brook et al., 1998; Burrough et al., 2007). This agrees with our observations of synchronous deposition of silica nodule-rich sands, diatomites, and carbonate-rich sands, reflecting stability in water flux. However, structural displacement along the northern MOZB flanks was also proposed to occur between 300 and 100 Ka, based on the preservation of archaeological artifacts of this age on paleo-Makgadikgadi lakebeds. This was interpreted to cause the deflection of the Cuando River from the Makgadikgadi Basin into the CE, forming a waterbody (Moore and Larkin, 2001; Moore et al., 2012). Furthermore, drying conditions that commenced at 110 ka following a wet period were inferred based on thermoluminescence dating and geochemical study of duricrusts in the Makgadikgadi Basin (Ringrose et al., 2005; Ringrose et al., 2009). Accordingly, a transition from a clast-dominated to chemical-dominated accumulation took place in the CE between 116 ± 9 and 81 ± 7 ka.

The last phase of carbonate precipitation and diatomite deposition in the CE documents an enduring waterbody that existed between 54 ± 5 and 11 ± 1 ka (Table 1, Figure 5). Lacustrine deposits from this period, centered at ~40 ka, were reported from all MOZ basins (summarized in Burrough et al., 2009), hinting at a vast expansion of the lacustrine/palustrine system. Holocene sediments have not been observed in the studied sections, and their absence is consistent with the climatically driven desiccation of a waterbody in the Makgadikgadi Basin in the early Holocene (Partridge et al., 1997; Burrough et al.,2009), possibly resulting in their erosion. Alternatively, such deposits could have also been removed due to the activation of faults

that occurred at ~6 ka in the CE, causing the diversion of drainage networks and inverted relief (Mokatse et al., 2022).

7. Conclusions

A combination of a mineralogical provenance study, optically stimulated luminescence (OSL) dating of alluvial and lacustrine deposits, and cosmogenic nuclide-based estimation of sand residence time was applied to chronologically constrain the landscape evolution in the Chobe Enclave, a tectonically active sector of the Okavango Rift Zone. The Chobe Enclave adjoins the thickest depocenter in the Makgadikgadi–Okavango–Zambezi Basin, which experienced significant down-warping at ~2.5 Ma. Cosmogenic nuclide-based modelling indicates that sand that was formed following this event is preserved on the elevated margins of the Makgadikgadi–Okavango–Zambezi Basin. Model results further suggest an additional event of landscape lowering occurring around 1.5 Ma, which probably corresponds to regional tectonism as most of the eolian Kalahari Sand was formed around this time and has been recycled since then in the semi-endorheic Kalahari Basin. This stage was followed by the accommodation of waterbodies within the Makgadikgadi–Okavango–Zambezi Basin, where their deposits of upper Pleistocene age are preserved. The last estimated episode of sand formation at 1.1 Ma marks the older limit for localized rifting in the Chobe Enclave, which probably occurred during the Middle Pleistocene Transition that took place between 1.2 and 0.75 Ma (Herbert, 2023).

Alluvial fans and waterbodies evolved within the depressed landscape of the Chobe Enclave, and their mineralogical signature suggests supply from both Zambezi and Cuando rivers, influenced by hydrological connectivity, climate, and tectonic activity. This alluvial system carried sand of different origin and diagenetic history than the older eolian sand that is structurally placed above the Chobe Enclave. Dating the alluvial sediments that were deposited in the evolved rift via OSL provided a younger time constraint for the incision. The earliest documented sedimentation in alluvial fan settings is dated as 252 ± 27 ka, representing the youngest age limit for a rifting episode in the Chobe Enclave. Finally, the subsidizing trough of the Chobe Enclave hosted waterbodies for at least ~140 ka, which were possibly connected with other waterbodies within the Makgadikgadi–Okavango–Zambezi Basin.

8. Acknowledgments

We are grateful for the preparation of cosmogenic nuclides, the practical comments, and the field missions conducted by Ari Matmon. We thank Tyrel Flugel for georectifying the isopach map. We share our gratitude to Guy Lang, Vincent Regard, and Sebastien Carretier for fruitful discussions and comments, Yigal Erel, Talila Kosh, Ehud Rudis, and Izhak Temkin for their company, guidance, and cooperation in the field, the Van Thuyne Ridge research center for their hospitality and logistic support, and the Botswana International University of Science and Technology for their fieldwork assistance. This work has been supported by a Swiss National Science Foundation grant no. 200021_172944 to E.P.V.

Open Research

Unless mentioned otherwise, the data presented in this paper is original. Mixing and similarity analyses based on mineralogical assemblages were performed after Garzanti et al. (2012) and Vezzoli and Garzanti (2009), respectively. OSL modelling for estimating dose rate and depositional age was performed via Mauz and Hoffmann (2014) Kreutzer et al. (2012, 2019, 2022), and Duller (2015). Cosmogenic nuclides modelling for residence time estimation was done using Cosmolian (Vainer and Ben Dor, 2021).

References

Agosta, E.A. and Compagnucci, R.H., 2016. Abrupt climate changes during the marine isotope stage 3 (MIS 3). Marine Isotope Stage 3 in Southern South America, 60 KA BP-30 KA BP, pp.81-106.

Andò, S., Garzanti, E., 2014. Raman spectroscopy in heavy-mineral studies. In: Scott, R.A., Smyth. H.R., Morton, A.C., Richardson, N. (Eds.), Sediment provenance studies in hydrocarbon exploration and production. Geological Society London, Special Publication 386, 395-412.

Baillieul, T.A., 1975. A reconnaissance survey of the cover sands in the Republic of Botswana. Journal of Sedimentary Research, 45(2), pp.494-503.

Bäumle, R., Himmelsbach, T. and Noell, U., 2019. Hydrogeology and geochemistry of a tectonically controlled, deep-seated and semi-fossil aquifer in the Zambezi Region (Namibia). Hydrogeology Journal, 27(3), pp.885-914.

Blair, T.C. and McPherson, J.G., 2009. Processes and forms of alluvial fans. In: Parsons, A.J., Abrahams, A.D. (eds) Geomorphology of Desert Environments. Springer, Dordrecht pp.413-467.

Bowman, D., 2019. Principles of alluvial fan morphology. Dordrecht: Springer, pp.151

Brook, G.A., Cowart, J.B., Brandt, S.A., 1998. Comparison of Quaternary environmental change in eastern and southern Africa using cave speleothem, tufa and rock shelter sediment data. Quaternary Deserts and Climate Change. G. Alsharhan, Whittle and Kendall. Rotterdam, Balkema.

Brook, G.A., Srivastava, P., Brook, F.Z., Robbins, L.H., Campbell, A.C. and Murphy, M.L., 2008. OSL chronology for sediments and MSA artefacts at the Toteng quarry, Kalahari Desert, Botswana. South African Archaeological Bulletin, 63(188), pp.151-158.

Brown, N.D., 2020. Which geomorphic processes can be informed by luminescence measurements?. Geomorphology, 367, p.107296.

Bufford, K.M., Atekwana, E.A., Abdelsalam, M.G., Shemang, E., Atekwana, E.A., Mickus, K., Moidaki, M., Modisi, M.P. and Molwalefhe, L., 2012. Geometry and faults tectonic activity of

713 the Okavango Rift Zone, Botswana: Evidence from magnetotelluric and electrical resistivity
714 tomography imaging. Journal of African Earth Sciences, 65, pp.61-71.

715 Burrough, S.L. and Thomas, D.S., 2013. Central southern Africa at the time of the African
716 Humid Period: a new analysis of Holocene palaeoenvironmental and palaeoclimate data.
717 Quaternary Science Reviews, 80, pp.29-46.

718 Burrough, S.L. and Thomas, D.S.G., 2008. Late Quaternary lake-level fluctuations in the
719 Mababe Depression: Middle Kalahari palaeolakes and the role of Zambezi inflows. Quaternary
720 Research, 69(3), pp.388-403.

721 Burrough, S.L., Thomas, D.S., Shaw, P.A. and Bailey, R.M., 2007. Multiphase quaternary
722 highstands at lake Ngami, Kalahari, northern Botswana. Palaeogeography, Palaeoclimatology,
723 Palaeoecology, 253(3-4), pp.280-299.

724 Chorowicz, J., 2005. The east African rift system. Journal of African Earth Sciences, 43(1–3),
725 379–410.

726 Clark, J.D., 1950. Part II – Archaeology. In: J.D. Clark (Editor), The Stone Age cultures of
727 Northern Rhodesia. Southern African Archaeological Society, Claremont, 30-131.

728 Cosgrove, G.I., Colombera, L. and Mountney, N.P., 2022. Quantitative analysis of aeolian
729 stratigraphic architectures preserved in different tectonic settings. Earth-Science Reviews,
730 p.104293.

731 Cotterill, F.P.D. and De Wit, M.J., 2011. Geoecodynamics and the Kalahari epeirogeny: linking
732 its genomic record, tree of life and palimpsest into a unified narrative of landscape evolution.
733 South African Journal of Geology, 114(3-4), pp.489-514.

734 Dauteuil, O., Jolivet, M., Dia, A., Murray-Hudson, M., Makati, K., Barrier, L., Bouhnik Le Coz,
735 M., Audran, A. and Radenac, A., 2021. Trace metal enrichments in water of the Okavango Delta
736 (Botswana): hydrological consequences. Geochemistry, Geophysics, Geosystems, 22(5).

737 Day, J.J., Bills, R. and Friel, J.P., 2009. Lacustrine radiations in African Synodontis catfish.
738 Journal of evolutionary biology, 22(4), pp.805-817.

739 DeCelles, P.G. and Cavazza, W., 1999. A comparison of fluvial megafans in the Cordilleran
740 (Upper Cretaceous) and modern Himalayan foreland basin systems. Geological Society of
741 America Bulletin, 111(9), pp.1315-1334.

742 Degering, D., Degering, A., 2020. Change is the only constant - time-dependent dose rates in
743 luminescence dating. Quaternary Geochronology 58, 101074.

744 Diaz, N., Armitage, S.J., Verrecchia, E.P. and Herman, F., 2019. OSL dating of a carbonate
745 island in the Chobe Enclave, NW Botswana. Quaternary Geochronology, 49, pp.172-176.

746 Dixey, F. H., 1956. The East African Rift System. Colonial Geol. Mineral Resources, 1, pp. 1–
747 71.

748 Doucouré, C.M. and de Wit, M.J., 2003. Old inherited origin for the present near-bimodal
749 topography of Africa. Journal of African Earth Sciences, 36(4), pp.371-388.

750 Du Toit, A.L., 1933. Crustal movements as a factor in the evolution of South Africa. S. Afr. J.
751 Sci. pp. 24, 88 – 101.

752 Duller, G.A.T., 2015. The Analyst software package for luminescence data: overview and recent
753 improvements. Ancient TL, 33(1), pp.35-42.

754 Durcan, J.A., King, G.E., Duller, G.A.T., 2015. DRAC: Dose Rate and Age Calculator for
755 trapped charge dating. Quaternary Geochronology 28, 54-61.

756 Esri. World Imagery Map. June, 2023.

757 Fairhead, J.D. and Girdler, R.W., 1969. How far does the rift system extend through Africa?.
758 Nature, 221(5185), pp.1018-1020.

759 Farr, T.G., Rosen, P.A., Caro, E., Crippen, R., Duren, R., Hensley, S., Kobrick, M., Paller, M.,
760 Rodriguez, E., Roth, L. and Seal, D., 2007. The shuttle radar topography mission. Reviews of
761 geophysics, 45(2).

762 Galbraith, R.F., Roberts, R.G., Laslett, G.M., Yoshida, H. and Olley, J.M., 1999. Optical dating
763 of single and multiple grains of quartz from Jinmium rock shelter, northern Australia: Part I,
764 experimental design and statistical models. Archaeometry, 41(2), pp.339-364.Garzanti E., 2017.
765 The maturity myth in sedimentology and provenance analysis. Journal of Sedimentary Research,
766 87, 353-365.

767 Garzanti, E., Andò, S., 2007. Heavy-mineral concentration in modern sands: implications for
768 provenance interpretation. In: Mange, M.A., Wright, D.T. (Eds.), Heavy Minerals in Use.
769 Elsevier, Amsterdam, Developments in Sedimentology Series 58, pp. 517-545.

770 Garzanti, E., Pastore, G., Resentini, A., Vezzoli, G., Vermeesch, P., Ncube, L., Niekerk, H.J.V.,
771 Jouet, G. and Dall'Asta, M., 2021. The segmented Zambezi sedimentary system from source to
772 sink: 1. Sand petrology and heavy minerals. The Journal of Geology, 129(4), pp. 343-369.

773 Garzanti, E., Pastore, G., Stone, A., Vainer, S., Vermeesch, P. and Resentini, A., 2022.
774 Provenance of Kalahari Sand: Paleoweathering and recycling in a linked fluvial-aeolian system.
775 Earth-Science Reviews, 224, p.103867.

776 Garzanti, E., Resentini, A., Vezzoli, G., Andò, S., Malusà, M., Padoan, M., 2012. Forward
777 compositional modelling of Alpine orogenic sediments. Sedimentary Geology, 280, 149-164.

778 Gierlowski-Kordesch, E.H., 2010. Lacustrine carbonates. Developments in sedimentology, 61,
779 pp.1-101.

780 Goodier, S.A., Cotterill, F.P., O'Ryan, C., Skelton, P.H. and de Wit, M.J., 2011. Cryptic diversity
781 of African tigerfish (Genus Hydrocynus) reveals palaeogeographic signatures of linked Neogene
782 geotectonic events. PloS one, 6(12), p.e28775.

Grove, A.T., 1969. Landforms and climatic change in the Kalahari and Ngamiland. The Geographical Journal, 135(2), pp.191-212.

Guérin, G., Mercier, N., Adamiec, G., 2011. Dose-rate conversion factors: update. Ancient TL 29, 5-8.

Gumbricht, T., McCarthy, T.S. and Merry, C.L., 2001. The topography of the Okavango Delta, Botswana, and its tectonic and sedimentological implications. South African Journal of Geology, 104(3), pp.243-264.

Haddon, I.G. and McCarthy, T.S., 2005. The Mesozoic–Cenozoic interior sag basins of Central Africa: the late-cretaceous–Cenozoic Kalahari and Okavango basins. Journal of African Earth Sciences, 43(1-3), pp.316-333.

Harvey, A. M., Stokes, M., Mather, A. and Whitfield, E., 2018. Spatial characteristics of the Pliocene to modern alluvial fan successions in the uplifted sedimentary basins of Almería, SE Spain: review and regional synthesis. Geological Society, London, Special Publications, 440(1), pp.65-77.

Harvey, A.M., 2002. The role of base-level change in the dissection of alluvial fans: case studies from southeast Spain and Nevada. Geomorphology, 45(1-2), pp.67-87.

Harvey, A.M., Mather, A.E. and Stokes, M., 2005. Alluvial fans: geomorphology, sedimentology, dynamics—introduction. A review of alluvial-fan research. Geological Society, London, Special Publications, 251(1), pp.1-7.

Herbert, T.D., 2023. The Mid-Pleistocene Climate Transition. Annual Review of Earth and Planetary Sciences, 51, pp.389-418.

Holz, M., Vilas-Boas, D.B., Troccoli, E.B., Santana, V.C. and Vidigal-Souza, P.A., 2017. Conceptual models for sequence stratigraphy of continental rift successions. In Stratigraphy & Timescales (Vol. 2, pp. 119-186). Academic Press.

Hooke, R.L., 1967. Processes on arid-region alluvial fans. The Journal of Geology, 75(4), pp.438-460.

Hubert, J.F., 1962. A zircon–tourmaline–rutile maturity index and the interdependence of the composition of heavy minerals assemblages with the gross composition and texture of sandstones. Journal of Sedimentary Petrology 32, 440-450.

Huntsman-Mapila, P., Kampunzu, A.B., Vink, B. and Ringrose, S., 2005. Cryptic indicators of provenance from the geochemistry of the Okavango Delta sediments, Botswana. Sedimentary Geology, 174(1-2), pp.123-148.

Huntsman-Mapila, P., Ringrose, S., Mackay, A.W., Downey, W.S., Modisi, M., Coetzee, S.H., Tiercelin, J.J., Kampunzu, A.B. and Vanderpost, C., 2006. Use of the geochemical and biological sedimentary record in establishing palaeo-environments and climate change in the Lake Ngami basin, NW Botswana. Quaternary International, 148(1), pp.51-64.

819 Keller, E.A. and DeVecchio, D.E., 2013. Tectonic geomorphology of active folding and
820 development of transverse drainages. In Tectonic Geomorphology (pp. 129-147). Elsevier Inc..

821 Kinabo, B.D., Atekwana, E.A., Hogan, J.P., Modisi, M.P., Wheaton, D.D. and Kampunzu, A.B.,
822 2007. Early structural development of the Okavango rift zone, NW Botswana. Journal of African
823 Earth Sciences, 48(2-3), pp.125-136.

824 Kinabo, B.D., Hogan, J.P., Atekwana, E.A., Abdelsalam, M.G. and Modisi, M.P., 2008. Fault
825 growth and propagation during incipient continental rifting: Insights from a combined
826 aeromagnetic and Shuttle Radar Topography Mission digital elevation model investigation of the
827 Okavango Rift Zone, northwest Botswana. Tectonics, 27(3), TC3013.

828 Kohl, C.P. and Nishiizumi, K., 1992. Chemical isolation of quartz for measurement of in-situ-
829 produced cosmogenic nuclides. Geochimica et cosmochimica acta, 56(9), pp.3583-3587.

830 Kreutzer, S., Burow, C., Dietze, M., Fuchs, M., Schmidt, C., Fischer, M., Friedrich, J., Mercier,
831 N., Philippe, A., Riedesel, S., Autzen, M., Mittelstrass, D., Gray, H., Galharret, J., 2022.
832 Luminescence: Comprehensive Luminescence Dating Data Analysis. R package version 0.9.20,
833 https://CRAN.R-project.org/package=Luminescence.

834 Kreutzer, S., Mauz, B., Martin, L., Mercier, N., 2019. 'RCarb': Dose Rate Modelling of
835 Carbonate-Rich Samples-an Implementation of Carb in R. Ancient TL 37.

836 Kreutzer, S., Schmidt, C., Fuchs, M.C., Dietze, M., Fischer, M., Fuchs, M., 2012. Introducing an
837 R package for luminescence dating analysis. Ancient TL 30, 1-8.

838 Lancaster, N., 1981. Paleoenvironmental implications of fixed dune systems in Southern Africa.
839 Palaeogeography, Palaeoclimatology, Palaeoecology, 33(4), pp.327-346.

840 Le Dortz, K., Meyer, B., Sébrier, M., Braucher, R., Bourlès, D., Benedetti, L., Nazari, H. and
841 Foroutan, M., 2012. Interpreting scattered in-situ produced cosmogenic nuclide depth-profile
842 data. Quaternary Geochronology, 11, pp.98-115.

843 Lecce, S.A., 1990. The alluvial fan problem. In: A.H. Rachocki, M. Church (Eds) Alluvial fans:
844 A field approach, Wiley, pp. 3-24.

845 Lustig, L.K., 1965. Clastic sedimentation in deep springs valley, California (Vol. 352). US
846 Government Printing Office.

847 Matmon, A., Hidy, A.J., Vainer, S., Crouvi, O., Fink, D., Erel, Y., Arnold, M., Aumaître, G.,
848 Bourlès, D., Keddadouche, K. and Horwitz, L.K., 2015. New chronology for the southern
849 Kalahari Group sediments with implications for sediment-cycle dynamics and early hominin
850 occupation. Quaternary Research, 84(1), pp.118-132.

851 Matmon, A., Nichols, K. and Finkel, R., 2006. Isotopic insights into smoothening of abandoned
852 fan surfaces, southern California. Quaternary Research, 66(1), pp.109-118.

Matmon, A., Schwartz, D.P., Finkel, R., Clemmens, S. and Hanks, T., 2005. Dating offset fans along the Mojave section of the San Andreas fault using cosmogenic 26Al and 10Be. Geological Society of America Bulletin, 117(5-6), pp.795-807.

McCarthy, T.S. and Ellery, W.N., 1995. Sedimentation on the distal reaches of the Okavango Fan, Botswana, and its bearing on calcrete and silcrete (ganister) formation. Journal of Sedimentary Research, 65(1a), pp.77-90.

McCarthy, T.S., 1993. The great inland deltas of Africa. Journal of African Earth Sciences (and the Middle East), 17(3), pp.275-291.

McCarthy, T.S., 2013. The Okavango Delta and its place in the geomorphological evolution of southern Africa. South African Journal of Geology, 116(1), pp.1-54.

McCarthy, T.S., Smith, N.D., Ellery, W.N., Gumbricht, T. 2002. The Okavango Delta - Semi-arid alluvial fan sedimentation related to incipient rifting. In: Renaut R.W. and Ashley G.M. (Eds), Sedimentation in Continental rifts. Society for Sedimentary Geology (SEPM), Special Publication, 73, 179-193.

McFarlane, M.J. and Eckardt, F.D., 2006. Lake Deception: a new Makgadikgadi palaeolake. Botswana Notes and Records, 38, pp.195-201.

McFarlane, M.J. and Eckardt, F.D., 2007. Palaeodune morphology associated with the Gumare fault of the Okavango graben in the Botswana/Namibia borderland: a new model of tectonic influence. South African Journal of Geology, 110(4), pp.535-542.

McFarlane, M.J. and Segadika, P., 2001. Archaeological evidence for the reassessment of the ages of the Makgadikgadi palaeolakes. Botswana Notes and Records, 33, 83-89.

Michon, L., Famin, V. and Quidelleur, X., 2022. Evolution of the East African Rift System from trap-scale to plate-scale rifting. Earth-Science Reviews, 231, p.104089.

Miller, R.M., Pickford, M. and Senut, B., 2010. The geology, palaeontology and evolution of the Etosha Pan, Namibia: Implications for terminal Kalahari deposition. South African Journal of Geology, 113(3), pp.307-334.

Modisi, M.P., Atekwana, E.A., Kampunzu, A.B. and Ngwisanyi, T.H., 2000. Rift kinematics during the incipient stages of continental extension: Evidence from the nascent Okavango rift basin, northwest Botswana. Geology, 28(10), pp.939-942.

Mokatse, T., Diaz, N., Shemang, E., Van Thuyne, J., Vittoz, P., Vennemann, T. and Verrecchia, E.P., 2022a. Landscapes and Landforms of the Chobe Enclave, Northern Botswana. In Landscapes and Landforms of Botswana (pp. 91-116). Cham: Springer International Publishing.

Mokatse, T., Vainer, S., Irving, J., Schmidt, C., Kgosidintsi, B., Shemang, E. and Verrecchia, E.P., 2022b. Geometry of sedimentary deposits and evolution of the landforms in the Chobe Enclave, Northern Botswana. Geomorphology, 415, p.108406.

888 Moore, A.E. and Cotterill, F.P.D., 2010. Victoria Falls: Mosi oa Tunya – the smoke that
889 thunders. In: P. Mignon (Editor), Geomorphological Landscapes. Springer, Berlin, 143-153.

890 Moore, A.E. and Larkin, P.A., 2001. Drainage evolution in south-central Africa since the
891 breakup of Gondwana. South African Journal of Geology, 104(1), pp.47-68.

892 Moore, A.E., 1999. A reappraisal of epeirogenic flexure axes in southern Africa. South African
893 Journal of Geology, 102(4), pp.363-376.

894 Moore, A.E., Cotterill, F.P., Main, M.P. and Williams, H.B., 2007. The zambezi river. Large
895 rivers: geomorphology and management, pp.311-332.

896 Moore, A.E., Cotterill, F.P.D. and Eckardt, F.D., 2012. The evolution and ages of Makgadikgadi
897 palaeo-lakes: consilient evidence from Kalahari drainage evolution south-central Africa. South
898 African Journal of Geology, 115(3), pp.385-413.

899 Murray, A., Arnold, L.J., Buylaert, J.-P., Guérin, G., Qin, J., Singhvi, A.K., Smedley, R.,
900 Thomsen, K.J., 2021. Optically stimulated luminescence dating using quartz. Nature Reviews
901 Methods Primers 1, 1-31.

902 Murray, A.S. and Wintle, A.G., 2000. Luminescence dating of quartz using an improved single-
903 aliquot regenerative-dose protocol. Radiation measurements, 32(1), pp.57-73.

904 Nash, D.J., Meadows, M.E. and Gulliver, V.L., 2006. Holocene environmental change in the
905 Okavango Panhandle, northwest Botswana. Quaternary Science Reviews, 25(11-12), pp.1302-
906 1322.

907 Nathan, R.P., Mauz, B., 2008. On the dose-rate estimate of carbonate-rich sediments for trapped
908 charge dating. Radiation Measurements 43, 14-25.

909 Nielsen, L.H., Petersen, H.I., Thai, N.D., Duc, N.A., Fyhn, M.B.W., Boldreel, L.O., Tuan, H.A.,
910 Lindstrom, S. and Hien, L.V., 2007. A Middle–Upper Miocene fluvial–lacustrine rift sequence in
911 the Song Ba Rift, Vietnam: an analogue to oil-prone, small-scale continental rift basins.
912 Petroleum Geoscience, 13(2), pp.145-168.

913 Olsen, P.E., Kent, D.V., Cornet, B., Witte, W.K. and Schlische, R.W., 1996. High-resolution
914 stratigraphy of the Newark rift basin (early Mesozoic, eastern North America). Geological
915 Society of America Bulletin, 108(1), pp.40-77.

916 Oriolo, S. and Becker, T., 2018. The Kalahari craton, southern Africa: from Archean crustal
917 evolution to Gondwana amalgamation. Geology of southwest Gondwana, pp.133-159.

918 Owen, L. A., Tectonic Geomorphology: A Perspective. Treatise on Geomorphology (Second
919 Edition), pp. 1-12. https://doi.org/10.1016/B978-0-12-818234-5.00155-3

920 Partridge, T.C., 1993. The evidence for Cainozoic aridification in southern Africa. Quaternary
921 International, 17, pp.105-110.

Partridge, T.C., Demenocal, P.B., Lorentz, S.A., Paiker, M.J. and Vogel, J.C., 1997. Orbital forcing of climate over South Africa: a 200,000-year rainfall record from the Pretoria Saltpan. Quaternary Science Reviews, 16(10), pp.1125-1133.

Pastier, A.M., Dauteuil, O., Murray-Hudson, M., Moreau, F., Walpersdorf, A. and Makati, K., 2017. Is the Okavango Delta the terminus of the East African Rift System? Towards a new geodynamic model: Geodetic study and geophysical review. Tectonophysics, 712, pp.469-481.

Paulssen, H., Micallef, T., Bouwman, D.R., Ruigrok, E., Herman, M.W., Fadel, I., van der Meijde, M., Kwadiba, M., Maritinkole, J. and Ntibinyane, O., 2022. Rifting of the Kalahari Craton through Botswana? New seismic evidence. Journal of Geophysical Research: Solid Earth, 127(4), p.e2021JB023524.

Placzek, C.J., Matmon, A., Granger, D.E., Quade, J. and Niedermann, S., 2010. Evidence for active landscape evolution in the hyperarid Atacama from multiple terrestrial cosmogenic nuclides. Earth and Planetary Science Letters, 295(1-2), pp.12-20.

Podgorski, J.E., Green, A.G., Kgotlhang, L., Kinzelbach, W.K., Kalscheuer, T., Auken, E. and Ngwisanyi, T., 2013. Paleo-megalake and paleo-megafan in southern Africa. Geology, 41(11), pp.1155-1158.

Porat, N., Amit, R., Enzel, Y., Zilberman, E., Avni, Y., Ginat, H. and Gluck, D., 2010. Abandonment ages of alluvial landforms in the hyperarid Negev determined by luminescence dating. Journal of Arid Environments, 74(7), pp.861-869.

Reeves, C.V., 1972. Rifting in the Kalahari?. Nature, 237(5350), pp.95-96.

Regard, V., Carretier, S., Boeglin, J.L., Ngoupayou, J.R., Dzana, J.G., Bedimo, J.P., Riotte, J. and Braun, J.J., 2016. Denudation rates on cratonic landscapes: Comparison between suspended and dissolved fluxes, and 10Be analysis in the Nyong and Sanaga River basins, South Cameroon. Earth Surface Processes and Landforms, 41(12), pp.1671-1683.

Ringrose, S., Harris, C., Huntsman-Mapila, P., Vink, B.W., Diskins, S., Vanderpost, C. and Matheson, W., 2009. Origins of strandline duricrusts around the Makgadikgadi Pans (Botswana Kalahari) as deduced from their chemical and isotope composition. Sedimentary Geology, 219(1-4), pp.262-279.

Ringrose, S., Huntsman-Mapila, P., Downey, W., Coetzee, S., Fey, M., Vanderpost, C., Vink, B., Kemosidile, T. and Kolokose, D., 2008. Diagenesis in Okavango fan and adjacent dune deposits with implications for the record of palaeo-environmental change in Makgadikgadi–Okavango–Zambezi basin, northern Botswana. Geomorphology, 101(4), pp.544-557.

Ringrose, S., Huntsman-Mapila, P., Kampunzu, H., Downey, W.D., Coetzee, S., Vink, B., Matheson, W., Vanderpost, C., 2005. Geomorphological and geochemical evidence for palaeo feature formation in the northern Makgadikgadi sub-basin, Botswana. Palaeogeog. Palaeoclim. Palaeoecol. 217, 265–287.

Ritter, J.B., Miller, J.R., Enzel, Y. and Wells, S.G., 1995. Reconciling the roles of tectonism and climate in Quaternary alluvial fan evolution. Geology, 23(3), pp.245-248.

Scheinert, C., Wasklewicz, T. and Staley, D., 2012. Alluvial fan dynamics–revisiting the field. Geography Compass, 6(12), pp.752-775.

Schmidt, G., Franchi, F., Salvini, F., Selepeng, A.T., Luzzi, E., Schmidt, C. and Atekwana, E.A., 2023. Fault controlled geometries by inherited tectonic texture at the southern end of the East African Rift System in the Makgadikgadi Basin, northeastern Botswana. Tectonophysics, 846, p.229678.

Scholz, C.H., Koczynski, T.A. and Hutchins, D.G., 1976. Evidence for incipient rifting in southern Africa. Geophysical Journal International, 44(1), pp.135-144.

Shaw, P.A. and Thomas, D.G., 1992. Geomorphology, sedimentation, and tectonics in the Kalahari Rift. Israel journal of earth-sciences, 41(2-4), pp.87-94.

Shaw, P.A. and Thomas, D.S.G., 1988. Lake Caprivi: a late Quaternary link between the Zambezi and middle Kalahari drainage systems. Zeitschrift für Geomorphologie, pp.329-337.

Shaw, P.A., Bateman, M.D., Thomas, D.S. and Davies, F., 2003. Holocene fluctuations of Lake Ngami, Middle Kalahari: chronology and responses to climatic change. Quaternary International, 111(1), pp.23-35.

Shaw, P.A., Thomas, D.S. and Nash, D.J., 1992. Late Quaternary fluvial activity in the dry valleys (mekgacha) of the Middle and Southern Kalahari, southern Africa. Journal of Quaternary Science, 7(4), pp.273-281.

Stanistreet, I.G. and McCarthy, T.S., 1993. The Okavango Fan and the classification of subaerial fan systems. Sedimentary geology, 85(1-4), pp.115-133.

Stewart, B.A. and Jones, S.C., 2016. Africa from MIS 6-2: the florescence of modern humans. Africa from MIS 6-2: Population Dynamics and Paleoenvironments, pp.1-20.

Stock, J.D., 2013. Waters divided: a history of alluvial fan research and a view of its future. In: Shroder, J. (Editor in Chief), Wohl, E. (Ed.), Treatise on Geomorphology. Academic Press, San Diego, CA, vol. 9, Fluvial

Stokes, S., Haynes, G., Thomas, D.S.G., Horrocks, J.L., Higginson, M. and Malifa, M., 1998. Punctuated aridity in southern Africa during the last glacial cycle: the chronology of linear dune construction in the northeastern Kalahari. Palaeogeography, Palaeoclimatology, Palaeoecology, 137(3-4), pp.305-322.

Terrizzano, C.M., Morabito, E.G., Christl, M., Likerman, J., Tobal, J., Yamin, M. and Zech, R., 2017. Climatic and Tectonic forcing on alluvial fans in the Southern Central Andes. Quaternary science reviews, 172, pp.131-141.

992 Thomas, D.S., O'Connor, P.W., Bateman, M.D., Shaw, P.A., Stokes, S. and Nash, D.J., 2000.
993 Dune activity as a record of late Quaternary aridity in the Northern Kalahari: new evidence from
994 northern Namibia interpreted in the context of regional arid and humid chronologies.
995 Palaeogeography, Palaeoclimatology, Palaeoecology, 156(3-4), pp.243-259.

996 Vainer, S. and Ben Dor, Y., 2021. The Cosmolian program for simulating aeolian dynamics and
997 its application to central Australia. Earth Surface Processes and Landforms, 46(9), pp.1631-1639.

998 Vainer, S., Dor, Y.B. and Matmon, A., 2018a. Coupling cosmogenic nuclides and luminescence
999 dating into a unified accumulation model of aeolian landforms age and dynamics: The case study
1000 of the Kalahari Erg. Quaternary Geochronology, 48, pp.133-144.

1001 Vainer, S., Erel, Y. and Matmon, A., 2018b. Provenance and depositional environments of
1002 Quaternary sediments in the southern Kalahari Basin. Chemical Geology, 476, pp.352-369.

1003 Vainer, S., Matmon, A., Ben Dor, Y., Verrecchia, E.P., Eckardt, F. and ASTER Team, 2022.
1004 Eolian chronology reveals causal links between tectonics, climate, and erg generation. Nature
1005 Communications, 13(1), p.5714.

1006 Vainer, S., Matmon, A., Erel, Y., Hidy, A.J., Crouvi, O., De Wit, M., Geller, Y. and ASTER
1007 Team, 2021. Landscape responses to intraplate deformation in the Kalahari constrained by
1008 sediment provenance and chronology in the Okavango Basin. Basin Research, 33(2), pp.1170-
1009 1193.

1010 Vandenberghe, D., De Corte, F., Buylaert, J.P., Kučera, J., Van den haute, P., 2008. On the
1011 internal radioactivity in quartz. Radiation Measurements 43, 771-775.

1012 Vezzoli, G., Garzanti, E., 2009. Tracking paleodrainage in Pleistocene foreland basins. The
1013 Journal of Geology, 117, 445-454.

1014 Viseras, C., Calvache, M.L., Soria, J.M. and Fernández, J., 2003. Differential features of alluvial
1015 fans controlled by tectonic or eustatic accommodation space. Examples from the Betic
1016 Cordillera, Spain. Geomorphology, 50(1-3), pp.181-202.

1017 Walker, T.R. and McKee, E.D., 1979. Red color in dune sand. United States Geological Survey
1018 Professional Papers, 1052, pp.61-81.

1019 Wang, L., D'odorico, P., Ringrose, S., Coetzee, S. and Macko, S.A., 2007. Biogeochemistry of
1020 Kalahari sands. Journal of Arid Environments, 71(3), pp.259-279.

1021 Warren, J.K., 2010. Evaporites through time: Tectonic, climatic and eustatic controls in marine
1022 and nonmarine deposits. Earth-Science Reviews, 98(3-4), pp.217-268.

1023 Watchman, A.L. and Twidale, C.R., 2002. Relative and 'absolute' dating of land surfaces. Earth-
1024 Science Reviews, 58(1-2), pp.1-49.

1025 Wilkinson, J., M., Miller, R., Eckardt, F., & Kreslavsky, M., 2023. Megafans of the Northern
1026 Kalahari Basin (Angola, Botswana, Namibia, Zambia). In J. Wilkinson & Y. Gunnell (Eds.),
1027 Fluvial Megafans on Earth and Mars (pp. 48-77). Cambridge: Cambridge University Press.

1028 Wright, V., Canales, J.P., de'Enremont, N., Matende, K., Moffat, L., Giosan, L., Laletsang, K.,
1029 Mapeo, R., Behn, M. and Ivory, S., 2021. Tectonostratigraphy of the northern Okavango Delta
1030 and Rift Zone, Botswana. Earth-ArXiv, https://doi.org/10.31223/X5W60J

1031 Young, M.J., Gawthorpe, R.L. and Sharp, I.R., 2000. Sedimentology and sequence stratigraphy
1032 of a transfer zone coarse-grained delta, Miocene Suez Rift, Egypt. Sedimentology, 47(6),
1033 pp.1081-1104.

1034 Yu, Y., Liu, K.H., Huang, Z., Zhao, D., Reed, C.A., Moidaki, M., Lei, J. and Gao, S.S., 2017.
1035 Mantle structure beneath the incipient Okavango rift zone in southern Africa. Geosphere, 13(1),
1036 pp.102-111.